

2015

LPI SUMMER INTERN PROGRAM IN PLANETARY SCIENCE

Papers Presented at the

31st Annual Summer Intern Conference

August 6, 2015 - Houston, TX



LUNAR AND
PLANETARY
INSTITUTE



Papers Presented at the

Thirty-First Annual Summer Intern Conference

**August 6, 2015
Houston, Texas**

2015 Summer Intern Program for Undergraduates
Lunar and Planetary Institute

Sponsored by
Lunar and Planetary Institute
NASA Johnson Space Center



LUNAR AND
PLANETARY
INSTITUTE



Compiled in 2015 by
Meeting and Publication Services
Lunar and Planetary Institute
USRA Houston
3600 Bay Area Boulevard, Houston TX 77058-1113

The Lunar and Planetary Institute is operated by the Universities Space Research Association under a cooperative agreement with the Science Mission Directorate of the National Aeronautics and Space Administration.

Any opinions, findings, and conclusions or recommendations expressed in this volume are those of the author(s) and do not necessarily reflect the views of the National Aeronautics and Space Administration.

Material in this volume may be copied without restraint for library, abstract service, education, or personal research purposes; however, republication of any paper or portion thereof requires the written permission of the authors as well as the appropriate acknowledgment of this publication.

HIGHLIGHTS

Special Activities

Date	Activity	Location
June 1	Lunar Curatorial and Stardust Lab Tour	NASA JSC
June 11	USRA Family BBQ Picnic	USRA/LPI
July 9	Meteorite Lab Tour	NASA JSC
July 16	Human Exploration Research Analog (HERA)/Morpheus	NASA JSC
July 17	LPI Science Staff Research Presentations	USRA/LPI
July 20	Annual Safety Training	USRA/LPI

LPI Summer Intern Program 2015 — Brown Bag Seminars

Wednesdays, 12:00 noon–1:00 p.m., USRA/LPI

Date	Speaker	Topic	Location
June 3	Paul Schenk	Dwarf Planets	Hess Conference Room
June 10	Donn Liddle	Virtual Extraterrestrial Samples	Hess Conference Room
June 17	Justin Simon	Protoplanetary Disk	Hess Conference Room
June 24	David Kring	Future Lunar Missions	Hess Conference Room
July 1	LPI Interns	Mid-Term Intern Reports	Hess Conference Room
July 7	Don Pettit	Living and Working in Space	Lecture Hall
July 8	Walter Kiefer	Planetary Interiors	Hess Conference Room
July 15	Buck Sharpton	Impact Cratering	Hess Conference Room
July 22	Steve Clifford	Water on Mars	Hess Conference Room
July 29	Aaron Burton	Meteorite Organics	Hess Conference Room
August 6	Andy Shaner	Education and Public Outreach	Hess Conference Room

LPI Summer Intern Tag Up and Science Fiction Film Series

Thursdays, 6:30 p.m., USRA/LPI

Date	Title	Location
June 11	Sunshine	Hess Conference Room
June 16	When Worlds Collide	Hess Conference Room
June 18	Forbidden Planet	Hess Conference Room
June 23	Dark City	Hess Conference Room
June 25	The Core	Hess Conference Room
July 2	Close Encounters of the Third Kind	Hess Conference Room
July 9	Fish Story	Hess Conference Room

AGENDA

- 8:00 a.m. **BREAKFAST**
- 8:25 a.m. Introductory Remarks by Drs. Stephen Mackwell, Paul Spudis, and David Draper
- 8:30 a.m. **TIMOTHY CAO, University of California, Merced**
(Advisors: Aaron Burton and Keiko Nakamura-Messenger)
Nanometer and Milligram Scale Analyses of Organics in CR Chondrites [#4007]
- 8:50 a.m. **CHRISTOPHER DONALDSON, University of Colorado Boulder**
(Advisor: Paul Niles)
Ultra-Low Temperature Acid Alteration of Silicates [#4009]
- 9:10 a.m. **ROBERT TREVOR GOLDMAN, Pomona College**
(Advisor: Walter Kiefer)
Constraining Lunar Thermal Evolution with Gravity Models of Elastic Flexure of Impact Basin Rim Topography [#4008]
- 9:30 a.m. **MYA ANN HABERMANN, University of Georgia**
(Advisors: Asmaa Boujibar, Kevin Righter, and Lisa Danielson)
Partitioning of U, Th, and K Between Silicate and Metal Under Reducing Conditions: Implications for Mercury's Differentiation [#4003]
- 9:50 a.m. **JESSICA MARIE JOHNSON, Central Connecticut State University**
(Advisors: Mike Zolensky and David Kring)
A Mineralogic and Petrographic Investigation of Unique Foreign Clasts in 3 Ordinary Chondrite Samples [#4004]
- 10:10 a.m. **ELEANOR CARMEN MCINTOSH, University of South Carolina**
(Advisors: Jennifer Rapp and Dave Draper)
Rare Earth Element Partitioning in Lunar Minerals: An Experimental Study [#4012]
- 10:30 a.m. **BREAK**
- 10:40 a.m. **ALEXANDRA BOBIAK NAGURNEY, Lafayette College**
(Advisors: Allan Treiman and Paul Spudis)
Petrology, Bulk Composition, and Provenance of Meteorite NWA5000 [#4002]
- 11:00 a.m. **PATRICK RICHARD PHELPS, University of Tulsa**
(Advisor: David Kring)
LL-Chondrite DOM-10092: A Shock-Metamorphosed Sample from an Impact-Modified Asteroid [#4010]

- 11:20 a.m. **MALGORZATA URSZULA SLIZ, The University of Manchester**
(Advisor: Paul Spudis)
Geology of the Deposits of the Lunar Crisium Basin [#4001]
- 11:40 a.m. **JOANNA SZCZESZEK, Adam Mickiewicz University in Poznań**
(Advisors: Paul Byrne, Francesca Scipioni, Trudi Hoogenboom, and Paul Schenk)
Characterizing Rayed Craters on Mercury and Ganymede [#4005]
- 12:00 p.m. **CHRISTIAN TAI UDOVICIC, University of Toronto**
(Advisors: Georgiana Kramer and Erika Harnett)
Lunar Swirls: Insights from Particle Tracking Simulations at Mare Marginis and NW of Apollo [#4011]
- 12:20 p.m. **ALLISON VANCE, Beloit College**
(Advisors: Roy Christoffersen and Lindsay Keller)
Evolution of Shock Melt Compositions in Lunar Regoliths [#4006]
- 12:40 p.m. **LUNCH**

CONTENTS

Nanometer and Milligram Scale Analyses of Organics in CR Chondrites <i>T. D. Cao , K. Nakamura-Messenger , A. S. Burton , and E. L. Berger</i>	1
Ultra-Low Temperature Acid Alteration of Silicates <i>C. Donaldson and P. B. Niles</i>	4
Constraining Lunar Thermal Evolution with Gravity Models of Elastic Flexure of Impact Basin Rim Topography <i>R. T. Goldman and W. S. Kiefer</i>	7
Partitioning of U, Th, and K Between Silicate and Metal Under Reducing Conditions: Implications for Mercury's Differentiation <i>M. Habermann , A. Boujibar , K. Righter , and L. Danielson</i>	10
A Mineralogic and Petrographic Investigation of Unique Foreign Clasts in 3 Ordinary Chondrite Samples <i>J. M. Johnson , M. E. Zolensky , Q. Chan , and D. A. Kring</i>	13
Rare Earth Element Partitioning in Lunar Minerals: An Experimental Study <i>E. C. McIntosh , J. F. Rapp , and D. S. Draper</i>	16
Petrology, Bulk Composition, and Provenance of Meteorite NWA5000 <i>A. B. Nagurney , A. H. Treiman , and P. D. Spudis</i>	19
LL-Chondrite DOM-10092: A Shock-Metamorphosed Sample from an Impact-Modified Asteroid <i>P. R. Phelps and D. A. Kring</i>	22
Geology of the Deposits of the Lunar Crisium Basin <i>M. U. Sliz and P. D. Spudis</i>	25
Characterizing Rayed Craters on Mercury and Ganymede <i>J. Szczeszek , T. Hoogenboom , F. Scipioni , P. Schenk , K. Johnson , and P. Byrne</i>	28
Lunar Swirls: Insights from Particle Tracking Simulations at Mare Marginis and NW of Apollo <i>C. J. Tai Udovicic , G. Y. Kramer , and E. M. Harnett</i>	31
Evolution of Shock Melt Compositions in Lunar Regoliths <i>A. M. Vance , R. Christoffersen , and L. P. Keller</i>	34

NANOMETER AND MILLIGRAM SCALE ANALYSES OF ORGANICS IN CR CHONDRITES

T. D. Cao¹, K. Nakamura-Messenger², A. S. Burton², E. L. Berger³ ¹University of California, Merced, CA, tcao6@ucmerced.edu, ²Astromaterials Research and Exploration Science Division, NASA Johnson Space Center, Houston, TX, ³GeoControl Systems Inc – Jacobs JETS contract, NASA Johnson Space Center, Houston, TX, USA

Introduction: Primitive carbonaceous chondrites contain a wide range of organic material, ranging from soluble discrete molecules to insoluble nanoglobules of macromolecular carbon. The relationship between the soluble organic molecules, macromolecular organic material, and host minerals are poorly understood. Due to the differences in extractability of soluble and insoluble organic materials, analysis methods for each differ from each other and are often performed independently. The combination of soluble and insoluble analyses can provide a wider understanding on spatial distribution, and elemental, structural and isotopic composition of organic material in primitive meteorites. Furthermore, they can provide wider perspective on how extraterrestrial organic materials potentially contributed to the synthesis of life's essential compounds such as amino acids, sugar acids, activated phosphates and nucleobases [1,9].

Mineralogy and insoluble organic material such as nano-globules and carbon-rich matrix can be observed and measured by high resolution electron microscopy techniques such as SEM (Scanning Electron Microscope), Fluorescence Microscopy, TEM (Transmitted Electron Microscope), then later isotopic imaging using NanoSIMS (Nanoscale secondary ion mass spectrometry) [8]. Soluble organic materials such as amino acids, carboxylic acids, and hydroxy acids can be extracted out of the same meteorite sample using macroscale extraction techniques and analyzed using liquid or gas chromatography, equipped with fluorescence or mass spectrometry detector.

Using macroscale extraction and analysis techniques as well as microscale *in situ* measurements, we studied both insoluble and soluble organic material in two primitive CR carbonaceous chondrites. By performing these studies on samples from the same meteorites, we aim to improve our understanding of the relationship between the physical properties of meteorite minerals and soluble and insoluble organic matter.

Samples: Previous analyses of amino acids in CR chondrites have revealed that these meteorites are generally very rich in amino acids [4,5,10]. In particular, CR chondrites that have experienced less extensive aqueous alteration tend to be the most abundant in amino acids.

Two CR carbonaceous chondrites: MILLER RANGE (MIL) 090657 and BUCKLEY ISLAND (BUC) 10933 were selected for this study. These CR chondrites have not been extensively characterized, but based on available data and their petrographic descriptions, these CR chondrites appear to have experienced

minimal aqueous alteration [3]. There have been no organic studies reported in the literature for these specimens. They have relatively large available masses of ~130 g (MIL 090657, 19) and ~485 g (BUC 10933, 11), making sufficient masses available for soluble organic extraction. We acquired total mass of 1 g for each meteorite sample in our study.

Sample Preparation and Analysis Method:

Insoluble Organic Material Study: To prepare samples for both SEM and TEM analyses, fine grained dark fragments (50 – 100 μm) were carefully selected from each of the two specimen's matrices under a stereomicroscope. Matrix fragments were then embedded in low-viscosity epoxy resins. Thin sections of 70-100 nm-thickness were prepared using ultramicrotomy and deposited on TEM grids. Bright and dark-field imaging were obtained using a JEOL 2500SE field-emission scanning TEM (FE-STEM) at NASA Johnson Space Center. Instrument is equipped with an energy-dispersive X-ray detector (EDX) analysis system, capable of nanometer-scale compositional mapping to study insoluble carbonaceous organic globules.

The remaining potted sample in epoxy stubs were carbon coated for mineralogical observation using a Scanning Electron Microscope (SEM). SEM investigation was carried out using a JEOL 7600F SEM instrument at NASA Johnson Space Center. Due to epoxy low conductivity and outgassing, high resolution backscatter electron imaging and x-ray elemental mapping were not possible. Only spot analysis was possible using the attached EDS 2600 detector to capture *insitu* mineral and elemental content at areas of interest.

Soluble Organic Material Study: All glassware and ceramics were cleaned of organic material by baking at 500°C in air overnight. Solvents were purified using double distillation techniques. These precautionary steps reduce or eliminate the introduction of terrestrial organic contamination during the extraction procedure. Each sample (153 mg for MIL 090657 and 160 mg for BUC 10933) was crushed into a fine powder using cleaned mortars and pestles. They were then transferred to ampoules.

Extraction of amino acids was performed by adding 4 mL of Millipore ultrapure water (<4ppb TOC) to each ampoule, along with two procedural blank samples that only contained water. Ampoules were flame sealed and incubated for 24 hours at 100°C. The tubes were opened, the supernatant was decanted from the solids. Solids were washed twice with 1 mL of ultrapure water. Half

of the material was set aside to determine the abundance of free amino acids, while the other half was subjected to acid hydrolysis. Both sets of samples were dried under vacuum using a Savant SPD131DDA SpeedVac Concentrator centrifuge set at 1 mmHg overnight. The test tubes containing the dried samples to be hydrolyzed were placed inside clean test tubes and double-distilled 6M hydrochloric acid was added to the outside tube. The outer tube was then flame-sealed. Acid-containing sealed tubes were heated for 3 hours at 150°C. This process causes the acid hydrolysis of amino acid precursor molecules such as amides, lactams, and nitriles into free amino acids groups [1]. Both the acid-hydrolyzed and non-hydrolyzed samples were purified by cation exchange chromatography (BioRad PolyPrep column packed with AG-50W resin), and eluted indoubly distilled 2M NH₄OH. This column removed non-cationic organic material and metal ions.

The purified amino acids will be analyzed by Ultra High Performance Liquid Chromatography- Fluorescence (UHPLC-FD) and Mass Spectroscopy (LC-MS) to determine the abundances, and structural and isotopic compositions of the amino acids present in each sample.

Results:

In-situ Observations (Insoluble Organic Materials):

BUC 10933: The matrix fragments of BUC 10933 were dominated by fine grained pyroxene crystallines. Fe, Ni-metal grains along with abundance of sulfide grains (~10 μm in size) were scattered throughout the pyroxene matrix. Ultramicrotomed thin sections from six BUC 10933 matrix fragments we observed in TEM did not contain any nanoglobule or carbonaceous matter.

MIL 090657: There were two distinct types of lithologies identified among the matrix: 1) with sub-micron granular silicate crystallines (Fig.1A and B) and 2) amorphous silicates (Fig.1C). The matrix with granular silicate grains was filled with sub-micron scale elaborated carbonaceous material network, wrapping around silicate grains (Fig.1A). EDX analysis indicated that these granular silicate were olivine and pyroxene. Surrounding these grains was a network of carbonaceous materials ranging from smooth to spongy structure (Fig.1A and B). The ratio of carbonaceous matter and mineral grains is 1:1. The carbonaceous matter network appeared to connect amorphous silicates with granular silicates, although no individual globule was observed in this lithology.

In the amorphous silicate dominant lithology, only minor nanoglobules with less than 400 nm in size were identified among with non-globuler shape carbonaceous matters (Fig.1C).

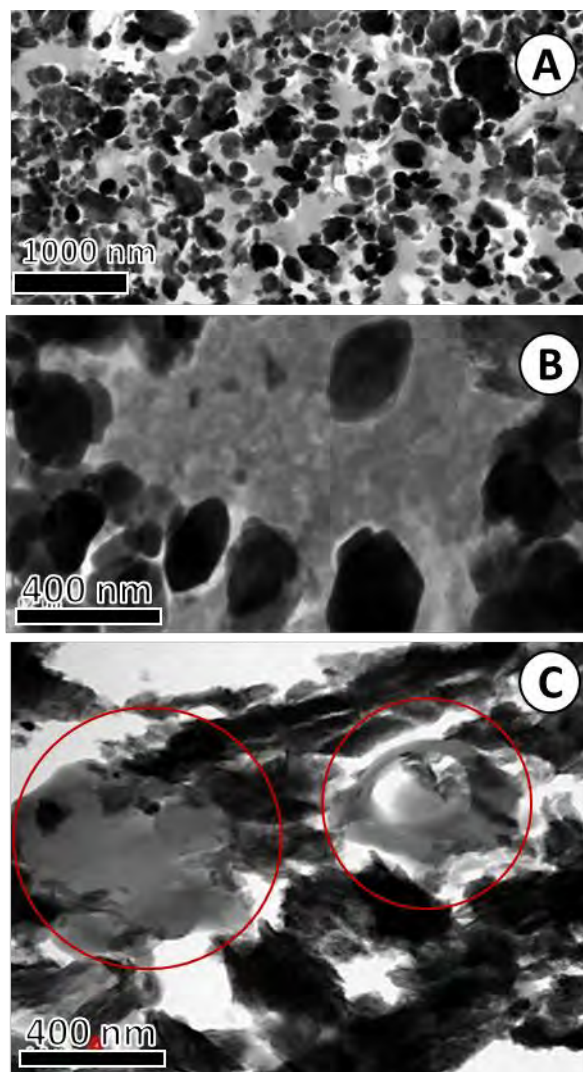


Figure 1: STEM Bright Field Images of MIL 090657 matrix showing variety of morphology of carbonaceous matters: **A:** the matrix with granular silicate grains (darker contrast) filled with carbonaceous material network. **B:** magnified view of carbonaceous matter network in Fig.1A showing spongy texture. **C:** hollow nanoglobule (right) and smooth carbonaceous matter (left) among amorphous silicate matrix.

Soluble Organic Materials:

Amino acid analyses of the MIL 090657 and BUC 10933 meteorites are planned, but have not yet been performed.

Discussions: Extensive insoluble organic matter has been reported from CR chondrite matrices, whether or not they were aqueously altered. Therefore in the CR2 chondrites in this study, we expected to find significant amounts of carbonaceous matter including nanoglobules.

In BUC 10933, the matrix is dominated by pyroxene and the presence of Fe, Ni-metal grains. This suggests that our BUC 10933 sample portion is more similar to a CV chondrite than a CR chondrite, which is consistent with the previous observation [7]. The absence of carbonaceous materials in in-situ analysis of BUC 10933 also support the reclassification. Our amino acid analyses should provide further insight into this difference as CV and CR chondrites have distinctive amino acid signatures [2,4]. Further mineralogical investigation is required for accurate classification on BUC 10933.

Elaborate networks of carbonaceous materials occupying half of the volume of matrix observed in the MIL 090657 have never been reported in any other primitive meteorite. The transition between amorphous and granular surfaces indicated that sample had gone under mild thermal/ aqueous alteration. The smooth morphology resembles reported carbonaceous morphology of CR3 chondrites [6], while spongy morphology resembles the CR2 “nanospheres with complex and vesicular hollow cores” [6]. The change in carbonaceous morphology suggests that the sample had experienced different level of alteration.

Soluble Organic Matter Hypothesis: Previous studies on soluble organic matter reported high concentration of amino acids, between 180,000 to 320,000 ppb in CR2 chondrites Elephant Moraine (EET) 92042 and GRA 95229 [4]. Amino acids in these meteorites were predominantly found to be α -amino isomers. Since our *in situ* studies of MIL 090657 suggests that the sample’s carbonaceous materials experienced different parent body processes than other CR2 and CR3 chondrites, we expect that MIL 090657’s amino acid concentration will be in between measured values of CR2 EET 92042 and CR3 QUE 99177. However, MIL 090657 is expected to contain higher relative abundances of non α -amino acid.

Based on our *insitu* study of BUC 10933, the sample’s amino acid composition might more closely reflect those of CV chondrites, with predominantly straight chain amino acids, and 10 to 100-fold lower amino acid abundances [2].

Conclusion:

We analyzed the mineralogy, soluble and insoluble organic materials in two meteorites nominally classified as CR2 chondrites. One meteorite, BUC 10933, appears to be more closely resemble CV chondrites rather than CR chondrites. The other meteorite, MIL 090657, was found to contain extensive networks of insoluble carbon that were dissimilar in morphology to what has previously been observed for CR3 chondrites, suggesting the sample experienced minor aqueous and thermal alteration. The effects of these parent body processes should also be observable in the planned amino acid analyses.

Acknowledgement:

T. D. Cao acknowledges financial support from the the LPI Summer Intern Program, Dr. Kathie Thomas-Keprta for assistance with Fluorescence Imaging, and Jessica Johnson, Chris Donaldson, Carrie McIntosh, Mya Haberman and Allison Vance for their valuable suggestions and comments throughout the program. A. S. Burton acknowledges support from the NASA Exobiology Early Career Fellowship program.

References: [1] Burton, A., et al. (2012) Chem. Soc. Rev., 41: 5459- 5472. [2] Burton, A. S., et al. (2012) Meteoritics & Planetary Science. 47: 374- 386. [3] Davidson, J. et al., (2015). LPSC XLVI, Abstract #1603. [4] Glavin, D. P., et al. (2010) Meteoritics & Planetary Science, 45: 1948-1972. [5] Martins, Z., et al. (2007) Earth and Planetary Science Letters. 270: 130- 136. [6] Matrajt, G., et al. (2012) Meteoritics & Planet. Sci., 47: 525-549. [7] McAdam, M. M., et al., (2015). LPSC XLVI, Abstract #2540. [8] Nakamura-Messenger, K., et al. (2006) Science, 314: 1439-1442. [9] Pizzarello S., et al. (2006) Meteorites and Early Solar System, 2: 626-63. [10] Pizzarello, S., Holmes, W. (2009) Geochimica et Cosmochimica Acta. 73:2150 - 2162.

ULTRA-LOW TEMPERATURE ACID ALTERATION OF SILICATES. C. Donaldson¹, P. B. Niles²;¹ Department of Geological Sciences, University of Colorado, Boulder, CO (chdo2490@colorado.edu);² Astromaterials Research and Exploration Science, NASA Johnson Space Center, Houston, TX.

Introduction: The history of Mars' past aqueous environments recorded in the alteration of its surface materials has the capacity to indicate whether life supporting climates have ever prevailed on the now cold and arid planet. There have been numerous models proposed in regard to the origin of the sulfate-bearing sedimentary deposits identified in several regions throughout Mars' mid to low latitudes, such as Meridiani Planum, yet there remain several problems with each interpretation [1, 2, 3].

Popular models for the sulfate rich deposits revolve around there having been warm enough conditions for longstanding liquid water accumulation. Nevertheless, several discrepancies with a warm, playa model for the formation of the Meridiani sediments during the Noachian do exist, including the faint young Sun paradox [4], and the lack of suitable greenhouse gases in order to compensate this effect [5]. These disparities, among several other chemical and compositional inconsistencies with many of the liquid water models [1, 2], could indicate that the initial geomorphic evidence for early warm and wet surface conditions might be more effectively explained by brief (< 1 My) occasional warming events rather than an extended period of warmth [6]. Nonetheless, a significant obstacle in proving the absence of a prolonged warm martian climate lies in explaining the sedimentary record which contains abundant sulfate minerals.

A model proposed by Niles and Michalski [3] suggests that acidic weathering of dust grain agglomerates compiled inside of vast ice deposits at temperatures well below 0 °C could result in substantial sulfate formation that would be re-deposited during the sublimation of the surrounding ice and subsequent aeolian reworking. However, in order for this model to be valid, acid-weathering of basaltic materials must occur at temperatures much lower than 0 °C. This has never before been demonstrated. It is hypothesized that the grain clusters would undergo acid induced alteration due to the formation of thin films of concentrated sulfuric acid created during eutectic freezing. In Niles et al. (2013) [7] laboratory experiments were conducted in order to test the feasibility of weathering olivine minerals at ultra-low temperature in the presence of acidic solutions. Their preliminary results demonstrated that if fine grained olivine on Mars was subjected to H₂SO₄ aerosols at temperatures above -40 °C, then it is

probable that they would weather into sulfate minerals in short time periods, with dissolution rates comparable to those of forsterite in a pH 4 solution at 25 °C. In this study we seek to understand whether sulfate minerals might form at temperatures much lower than previously thought. This study seeks to expand the preliminary work to other basaltic minerals including enstatite, labradorite, as well as basalt itself.

Methods: Along with incorporating additional basaltic minerals, in this study we wanted to directly compare ultra-low and average temperature alteration, so compositionally identical experiments were conducted at both -45°C and 15°C.

Starting minerals were ground and sieved to a <53µm grain size, sonicated in ethanol for 10 min., and had the finest particles decanted after the larger grains were allowed to settle. 0.5 mL of 0.5 M H₂SO₄ was added to 12 mL borosilicate glass Exetainers containing 10 g of acid-washed, 400 µm silica microspheres, and shaken to mix, theoretically yielding a ~9µm depth acidic coating on each microsphere.

	Average Grain Size (µm)	BET Surface Area (m ² /g)
Olivine	35	2.4
Enstatite	16	10.1
Labradorite	24	2.1
Basalt (unanalyzed)	-	-

After bringing all starting material to the desired temperatures, 50 mg aliquots of mineral substrate were added to their respective tubes, shaken to mix, and immediately returned to their target temperature. Most experiments were harvested at designated time intervals (0hr, 1d, 7d) by neutralizing/melting the contents with 10 mL of 0.1 M sodium acetate, shaking for 30 seconds, and promptly filtering the resultant mixture in order to obtain the solution for ICP-MS analysis. Control experiments bearing microspheres without minerals were included for each time interval. All but the 0hr experiments were run in duplicate and the averaged values are reported here. A number of other experiments had 100 mg aliquots of mineral substrate added, and were removed at 1 and 7 days to be either freeze dried or air dried, depending on their applicable target temperature. The resulting solid reaction products had their mineralogical properties investigated using SEM.

Results:

0hr solutions. In most cases, the 0hr mineral bearing solutions exhibited higher abundances of each of the elements than the 0hr control solutions which contained no minerals. Primarily, the exceptions to this were found in S, Al, and Na. In general, all of the relevant cations were present in higher abundance in the 15 °C 0hr experiments than in the -45 °C 0hr experiments.

Table 1. 0 hr Dissolved Element Abundances (ppm)

Temp.	Expt.	Mg	Fe	S	Si	Ca	Al	K
-45	Olivine	4.4	0.7	364.6	2.8	5.0	0.3	0.7
	Enstatite	4.2	0.2	331.1	1.3	42.7	0.2	0.9
	Labradorite	1.8	0.3	320.6	2.3	10.8	1.7	1.0
	Basalt	3.9	2.1	290.2	26.7	29.1	24.9	8.0
	Control	1.6	0.2	739.9	2.1	4.8	2.6	1.0
15	Olivine	9.9	1.7	370.0	6.8	6.1	0.4	0.8
	Enstatite	6.3	0.2	327.2	2.1	52.3	0.2	1.2
	Labradorite	2.5	0.4	330.8	2.7	12.8	2.4	1.4
	Basalt	6.4	4.2	290.7	51.4	40.3	57.0	16.0
	Control	2.6	0.3	766.7	3.2	9.5	3.7	1.6

1d solutions. Differences in the amount of dissolved species between the 1d and 0hr experiments show larger amounts of dissolved elements were present after 1d at both -45 °C and 15 °C (Table 2). However, in the basalt experiment there were significant losses in Si at both temperatures, and at 15 °C there was significant losses of S in the olivine experiment. There were larger concentrations of elements in the solutions from the 15 °C experiments. At both temperatures the control experiments exhibited a decrease in measured abundances in most elements compared to the 0hr controls.

Table 2. Dissolved Element Gain/Loss from 0hr to 1d (ppm)

Temp.	Expt.	Mg	Fe	S	Si	Ca	Al	K
-45	Olivine	0.5	0.1	-5.4	-0.4	-0.2	0.1	0.0
	Enstatite	1.4	0.2	276.9	-0.6	-3.4	0.2	0.2
	Labradorite	1.0	0.4	462.1	-0.1	0.3	2.1	0.5
	Basalt	1.4	0.7	376.8	-21.3	-3.2	19.9	7.3
	Control	-0.4	0.0	-434.7	-1.3	-0.9	-2.4	-0.4
15	Olivine	206.9	39.5	-89.2	44.3	0.5	0.2	-0.1
	Enstatite	19.6	2.3	291.8	2.8	1.3	0.4	1.2
	Labradorite	4.1	3.0	323.3	2.5	1.4	7.1	0.7
	Basalt	78.1	5.7	201.2	-43.8	2.8	-47.7	15.3
	Control	-0.7	0.0	-449.3	-1.8	-3.4	-3.3	-0.7

7d solutions. Mg, Fe, Ca, and Al concentrations were significantly larger, consistent with their respective mineral's chemical composition, in the solutions from the 7d experiments (Table 3). Similar to the 0hr-1d interval the 15 °C experiments showed larger concentrations of appropriate elements than the -45 °C experiments.

Table 3. Dissolved Element Gain/Loss from 0 hr to 7d (ppm)

Temp.	Expt.	Mg	Fe	S	Si	Ca	Al	K
-45	Olivine	9.2	0.9	-21.6	-1.8	4.9	1.6	0.6
	Enstatite	26.0	1.8	397.2	-0.5	165.3	1.5	2.5
	Labradorite	9.2	1.4	419.0	-0.2	34.9	12.1	3.4
	Basalt	29.6	17.1	490.8	-24.8	119.5	302.6	74.6
	Control	0.9	0.0	-432.1	-1.4	3.9	-0.7	0.2
15	Olivine	853.9	40.0	-7.9	-4.5	7.4	-0.4	0.6
	Enstatite	173.4	17.8	415.0	4.3	186.6	1.7	5.8
	Labradorite	31.8	20.0	415.6	4.4	57.0	74.6	5.9
	Basalt	414.2	116.5	298.0	-32.9	132.0	79.6	80.6
	Control	2.7	0.3	-437.7	-1.6	1.4	-1.5	-0.4

pH. The pH of the solutions was measured after addition of the Na-acetate buffer. Most solutions had a pH between 4.6 - 4.9. However, in the 15 °C basalt and olivine experiments, the measured pH of the 1d and 7d solutions exhibited an increase compared to the solutions collected after 0hr. The 1d and 7d basalt experiments had a pH of ~5.2 while the solutions from the olivine experiments increased from 5.9 at 1d to 6.4 at 7d. An orange precipitate was visible in the 15 °C 1d and 7d olivine solutions and a yellow tint was observed in the 15 °C 1d and 7d basalt solutions.

SEM Analysis. EDS analysis of the starting SiO₂ microspheres revealed a significant abundance of Na, with trace amounts of Al, Ca, and Mg also present. A needle-like Ca and S-rich, Si-poor phase was detected in both the enstatite and basalt experimental sets (Fig 2). A Mg and S-rich, Si-poor phase was positively identified in conjunction with olivine grains in the freeze dried -45 °C 1d and 7d experiments (Fig 3). Similar alteration products were also found in the air dried 15 °C 7d experiment.

XRD Analysis. XRD analysis was conducted on each of the starting materials. For the most part the samples were mineralogically pure, however one noticeable exception was the presence of apatite in low abundances within the enstatite starting material.

Discussion: Control experiments showed that there was a measurable contribution from all of the considered elements, likely arising from a combination of the silica microspheres, the borosilicate glass tubes, and the added solutions. Nevertheless, these contributions were minor compared to the mineral-bearing experiments (Tables 1-3). Higher abundances of dissolved Mg, Fe, and Ca in the 0 hr. mineral bearing experiments than was found in the 0hr control experiments demonstrates that measurable weathering occurred at the immediate onset of the experiments, likely due to the rapid dissolution of the smallest fraction of grains.

The mineral bearing 1d solutions indicated that weathering had continued to occur in both the -45 °C

and 15 °C experiments and substantial evidence for alteration was observed through SEM analysis. A decline in element abundance in the control experiments between 0hr and 1d may point to precipitation, however another possible explanation could be that variations in the contributions from the experiment materials resulted in slightly different abundances. 7d solutions showed considerably more evidence for weathering and SEM analysis confirmed this.

The main objective of this study was to demonstrate that weathering can occur at temperatures significantly below 0 °C for different mineral types that might be found on Mars. The results from the measurements of cation abundances in the 1d and 7d experiments compared to the controls suggest that significant weathering had occurred in the -45 °C experiments. Furthermore, SEM analysis of experimental products also revealed that substantial weathering of each mineral type was occurring.

Using the same method as Niles et al. (2013) [7], weathering rates have so far only been calculated for the olivine experiments (Figure 1). The calculated weathering rates for both -45 and 15 °C experiments are slower than previous results in Niles et al. (2013) [7], which were conducted at -40 °C. This suggests that experimental conditions and/or methods were not identical between the two experiments, potentially caused by differences in the specific surface area of the starting materials. Another possibility is suggested by pH measurements in the 15 °C olivine experiments which increased substantially compared to controls. This indicates substantial weathering occurred, however, this might have been obscured by precipitation of secondary minerals that were not later re-dissolved during the addition of the Na-acetate buffer solution. Precipitation of insoluble minerals during the experiment and after collection of the solution could have occurred, which would lower the measured elemental abundances and the apparent weathering rates.

The presence of minor apatite in the enstatite starting material provided an intriguing effect on the secondary mineralogy observed via SEM analysis (Fig 2-3). Ca-, S-rich secondary materials were predominant in the enstatite experiments while Mg-, S-rich secondary materials were predominant in the olivine experiments. This is likely due to the differences in solubility between Ca-sulfate and Mg-sulfate minerals showing that even in low water-rock environments, as simulated here, the presence of Ca in the system will result in the formation of Ca-sulfate minerals.

Conclusions: The results of the experiments indicated that weathering at extremely low temperatures (-45 °C) occurs. Even over the short experimental time-span substantial secondary materials were observed. The results for the -45 °C experiments showed significantly slower weathering rates, however the observed rates were largely comparable (Figure 1).

Figure 1.

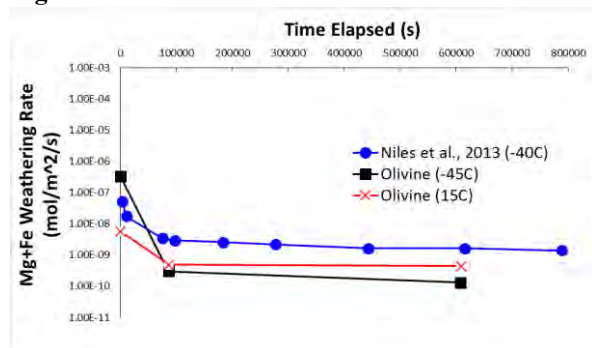


Figure 2. -45°C 1d enstatite expt. showing starting material (left) and Ca and S-rich, Si-poor alteration phase (right).

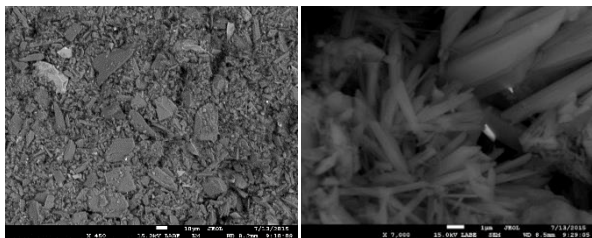
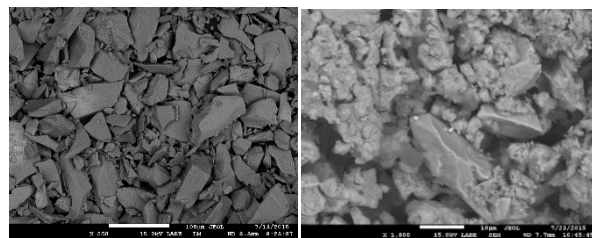


Figure 3. -45°C 7d olivine expt. showing starting material (left) and olivine grains surrounded by an Mg and S-rich, Si-poor alteration phase (right).



References: 1. McCollom, T. M. & Hynek, B. M. (2005) *Nature* 438, 1129-1131. 2. Knauth, L., et al. (2005) *Nature* 438, 1123-1128. 3. Niles P.B. and Michalski J. (2009) *Nature Geoscience*, 2, 215-220. 4. Gough D.O. (1981) *Solar Physics*, 74, 21-34. 5. Tian F., et al. (2010) *Earth and Planetary Science Letters*, 295, 412-418. 6. Gaidos E. and Marion G. (2003) *Journal of Geophysical Research-Planets*, 108. 7. Niles P.B., et al. (2013) *XLIV LPS*, Abstract # 2526.

CONSTRAINING LUNAR THERMAL EVOLUTION WITH GRAVITY MODELS OF ELASTIC FLEXURE OF IMPACT BASIN RIM TOPOGRAPHY. Robert T. Goldman¹ and Walter S. Kiefer², ¹Geology Department, Pomona College, Claremont, CA 91711 (rtg02011@mymail.pomona.edu), ²Lunar and Planetary Institute, Houston, TX 77058 (kiefer@lpi.usra.edu)

Introduction: Although the Moon is volcanically inactive today, it has experienced over 2 billion years of volcanic activity [1], as manifested in the lunar mare that cover roughly one-third of the Moon's nearside surface and 1% of its farside hemisphere [2]. Various investigators have used mantle convection models to learn about the Moon's global thermal evolution [e.g., 2, 3]. These studies show that as the lunar lithosphere thickens with time, it served to insulate the underlying mantle and thus extended the Moon's volcanic lifespan. In addition, the high concentration of radioactive material beneath the Procellarum KREEP Terrane on the northern part of the lunar nearside could explain the present-day volcanic dichotomy between its nearside and farside hemispheres. Understanding thermal structure on smaller scales is also important, for it affected the formation and evolution of large impact basins [e.g., 4]. Thus, understanding lunar thermal evolution is crucial for comprehending the Moon's geologic history.

It is important to test these thermal evolution models with observational constraints on lunar interior temperature and heat flux as a function of time. The thickness of the elastic lithosphere, which is the strong, outermost layer of a solid planet, depends on the temperature structure of the outer part of the planet [5]. One way to estimate lithospheric thickness is to quantify its flexural response to an applied gravitational load, such as a large volcano or mountain belt [e.g., 6]. This was successfully applied to Mars [7] and is now possible for the Moon for the first time due to the acquisition of high resolution gravity data by the GRAIL (Gravity Recovery and Interior Laboratory) mission [8]. An alternative approach to constraining lunar elastic thickness relies on modeling of the spatial distribution of tectonic structures [9, 10].

On the Moon, impact basins are rimmed by concentric mountain belts and ejecta deposits (estimated to be up to 2.9 km thick at the Cordillera ring of the Orientale basin [11]) that exert substantial loads on the underlying lithosphere. The magnitude of the gravity anomaly associated with rim topography and ejecta deposits depends on the lithospheric thickness at the time of the impact, with larger lithospheric thicknesses being associated with larger free-air gravity anomalies. Because the rim and ejecta blanket topography were created instantaneously on a geologic timescale, the inferred lithospheric thickness refers to a well-defined

moment in time, which facilitates using the flexure results as constraints on thermal evolution.

The goal of this study was to use recently acquired high resolution gravity and topography data for the Moon to estimate its lithospheric thickness at several locations and to infer its ancient thermal structure. We use GRAIL gravity model GRGM900C, which includes data from the low-altitude extended mission [12], which has a half-wavelength resolution of about 8 km and an amplitude uncertainty of less than 0.5 mGal. The highest resolution topography data come from the Lunar Orbiter Laser Altimeter aboard the Lunar Reconnaissance Orbiter [13], which has a spatial resolution of about 100 meters and a vertical uncertainty of less than 10 meters.

In this work, we model lithospheric flexure associated with the rims of three major impact basins (Orientale, Moscoviense, and Crisium). We focus our analysis on regions including and outside of the topographic rim for each basin (e.g., the Cordillera ring for Orientale). Hydrocode simulations of impact basin formation show that the central portion of each basin is heated to above the melting point of the mantle. However, this impact heating is negligible beyond the topographic basin rim, so the thickness of the underlying lithosphere in that region was not reset by the heat produced from the impact event [14]. Moreover, by focusing our attention outside of the topographic rim, we avoid the super-isostatic gravity structure associated with mascons [15], which would interfere with our ability to estimate lithospheric thickness near the basin center.

Methods: We generated global free-air gravity anomaly models of the Moon using the observed LOLA topography data [13] and the expected flexure resulting from that topography for given crustal thicknesses, elastic lithosphere thicknesses, and crustal densities. Flexure is calculated from a spherical thin-shell elastic flexure model [16] that incorporates both bending stresses and membrane stresses in the flexural force balance. Calculation of the gravity anomaly associated with the flexurally supported topography includes the effects of finite amplitude topography up to sixteenth order [17].

We then calculated the RMS misfits between our free-air gravity anomaly models and the observed GRAIL gravity data [12] over boxes with dimensions comparable to 10 degrees of latitude by 10 degrees of

longitude that sampled the rims of each impact basin (Orientale, Moscoviense, and Crisium). Each basin rim was sampled by six to eight boxes, each of which spanned a unique range of azimuths around the rim (see Figure 3). For each sampled region, RMS misfits were calculated between the observed and modeled gravity anomalies to determine the best-fit crustal density and elastic thickness beneath that area. We assume a global mean crustal thickness of 40 km, which is in the middle of the narrow range of crustal thicknesses (34-43 km) permitted by the combination of GRAIL gravity and Apollo seismic data [18]. Our results are not sensitive to the precise value of crustal thickness. Our results do depend on both the density of the topography and on the elastic lithosphere thickness, so we proceed using a two step process.

First, we constrain the density of the ejecta blanket outside of the basin rim by minimizing the RMS misfit for spherical harmonic degrees 180-500, corresponding to spatial wavelengths of 20-60 km. At these short wavelengths, gravitational attraction attenuates very rapidly with depth. As a result, at these harmonic degrees, the effects of lithospheric flexure and mantle density on the gravity anomalies are negligible, leaving crustal density as the only significant contributor to the gravity field.

Using the best fit crustal density for each analysis box, we determine lithospheric thickness from the gravity observations at spherical harmonic degrees 30-120, or spatial wavelengths of 90-360 km. Gravity anomalies at these harmonic degrees are primarily controlled by bending stresses associated with lithospheric flexure. Once the elastic lithosphere thickness is constrained, we can apply the moment-curvature correction [5] and use a lithosphere strength envelope to estimate the near surface thermal gradient and heat flux at the time of impact basin formation.

Density Results: We constrained the best-fit crustal density outside the Cordillera Ring of Orientale to fall between 2300 and 2400 kg m⁻³, with uncertainties spanning the range of 2210 to 2540 kg m⁻³. The best-fit crustal densities outside the rims of Moscoviense and Crisium span 2350 to 2450 kg m⁻³, with uncertainties ranging from 2230 to 2570 kg m⁻³ for Moscoviense and 2180 to 2590 kg m⁻³ for Crisium.

Figure 1 presents the RMS misfit results for Orientale. The density does not vary significantly with azimuth about the basin, which is consistent with the overall circular symmetry of the Orientale basin. The densities derived here are consistent with those that were based solely on lower resolution GRAIL Prime Mission observations [18]. The densities are also consistent with laboratory measurements of the bulk density of crystalline matrix breccias from the Fra Mauro

Formation, which was ejected from the Imbrium basin [19, 20].

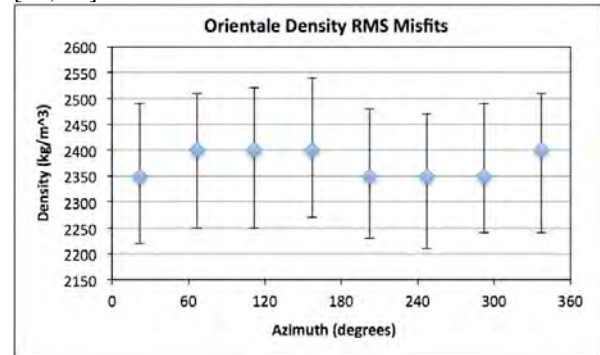


Figure 1. RMS density misfits calculated for the ejecta blanket outside of the Cordillera Ring of Orientale basin.

Figure 2 presents the RMS misfit results for Crisium basin. These results represent new work, as this region was not included in the density mapping of previous investigators [18]. The ejecta density around Crisium is similar to but slightly larger than those found for Orientale. This may be due to the gravitational influence of mare basalt in Mare Crisium near the edges of our analysis boxes. We omitted the regions on the southwest side of Crisium (azimuths between 180 and 270°) as any basin ejecta in these regions was flooded by later mare basalt volcanism from Mare Tranquillitatis.

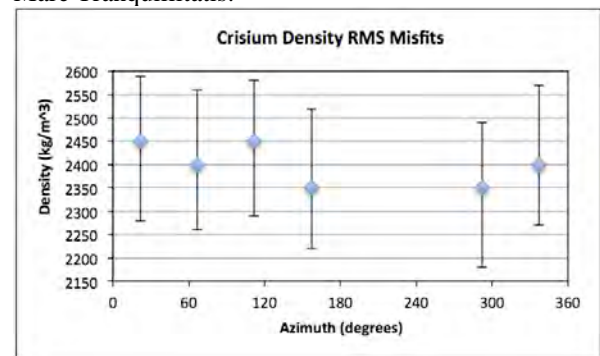


Figure 2. RMS density misfits calculated for the region outside of the rim of Crisium basin.

Elastic Thickness Results: We attempted to minimize the RMS misfit between our free-air anomaly gravity models and the gravity data for harmonic degrees 30-120 using our constrained values for crustal density. Although we used the same spatial boxes for this procedure as we did for finding the best-fit densities, the value of the RMS misfit did not change significantly over a span of 5 to 60 km in lithospheric thickness. Moreover, the residual gravity anomaly field has localized regions with very large residual amplitudes. Therefore, we could not constrain the lithospheric thickness outside any of the impact basin rims.

We are currently attempting to assess the cause of these unexpectedly large residuals using the spatial pattern of the residual gravity anomalies with respect to the basin structure. One possible cause of these large residual amplitudes could be the existence of faults that have offset the crust-mantle boundary outside the topographic rims of these basins, such as the Cordillera Ring of Orientale Basin [21, 22]. This offset would alter the gravity anomaly from that caused solely by lithospheric flexure of basin topography. If faults are found to exist around the Cordillera Ring or corresponding rims of other impact basins, then their presence can be accounted for in revised flexural models that may successfully constrain the lithospheric thickness, and from there the thermal profile, outside of the impact basin rims.

References: [1] Antonenko et al. (1995) *Earth Moon Planets*, 69, 141-172. [2] Laneuville et al. (2013) *JGR*, 118, 1435-1452. [3] Ziethe et al. (2009) *Planetary and Space Science*, 57, 784-796. [4] Potter et al. (2012) *GRL*, 39, L18203. [5] McNutt (1984) *JGR*, 89, 11180-11194. [6] Turcotte and Schubert (2002) *Geodynamics*, 2nd ed., Cambridge University Press, New York. [7] McGovern et al. (2002) *JGR*, 107, 5136. [8] Zuber et al. (2013) *Science*, 339, 668-671. [9] Comer et al. (1979) *Proc. Lunar Planet. Sci. Conf. 10th*, 2441-2463. [10] Solomon and Head (1980) *Reviews of Geophysics and Space Physics*, 18, 107-141. [11] Fassett et al. (2011) *GRL*, 38, L17201. [12] Lemoine et al. (2014) *GRL*, 41, 3382-3389. [13] Smith et al. (2010) *GRL*, 37, L18204. [14] Potter et al. (2013) *JGR: Planets*, 118, 963-979. [15] Melosh et al. (2013) *Science*, 340, 1552-1555. [16] Turcotte et al. (1981) *JGR*, 86, 3951-3959. [17] Wieczorek and Phillips (1998) *JGR*, 103, 1715-1724. [18] Wieczorek et al (2013) *Science*, 339, 671-675. [19] Kiefer et al. (2012) *GRL*, 39, L07201. [20] Kiefer et al. (2015) *LPSC 46*, Abstract #1711. [21] Kattoum and Andrews-Hanna (2013) *Icarus*, 226, 694-707. [22] Nahm et al. (2013) *JGR*, 118, 1-16.

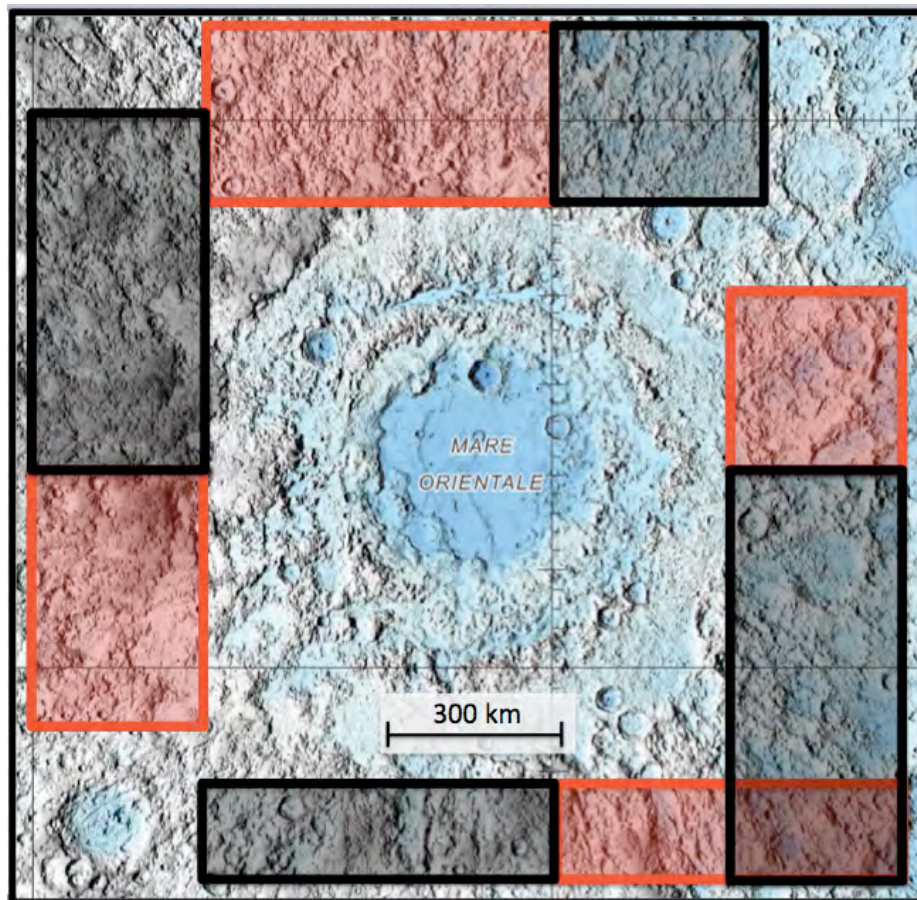


Figure 3. Map of regions outside the Cordillera Rim used to constrain density around Orientale basin.

Partitioning of U, Th, and K Between Silicate and Metal Under Reducing Conditions: Implications for Mercury's Differentiation

M. Habermann¹, A. Boujibar², K. Righter², L. Danielson³ ¹The University of Georgia, Athens, GA 30605, myanh@uga.edu; ²NASA Johnson Space Center, 2101 NASA Parkway, Houston, TX 77058, asmaa.boujibar@nasa.gov; Kevin.righter-1@nasa.gov; ³Jacobs JETS, NASA Johnson Space Center, 2101 NASA Pkwy, Houston, TX 77058, Lisa.r.danielson@nasa.gov.

Introduction: Prior to the MErcury Surface, Space ENvironment, GEochemistry, and Ranging (MESSENGER) mission it was thought that Mercury was depleted in volatiles. During planetary formation, the sun emitted strong solar winds and high heat, which are thought to have expelled a portion of the volatile elements from the inner solar system [1]. Thus, planets nearer to the sun are thought to be depleted in volatiles relative to planets further from the sun. This trend is supported by the compositional analyses and K/Th and K/U ratios of Venus, the Earth, and Mars [2]. However, the measured K/U and K/Th ratios for the surface of Mercury are much higher than expected, based on Mercury's distance from the sun [2].

K/U and K/Th ratios represent the overall volatile content of the planet, because potassium is a moderately volatile element compared against two refractory elements, uranium and thorium. Additionally, K is a large ion lithophile element, and U and Th are high field strength elements, incompatible elements, therefore the ratios between them are not expected to be affected by differentiation. K/U and K/Th are also important for understanding the heat budget and cooling rate of Mercury, as U and Th are radioactive.

It is possible that the K/Th and K/U ratios on the surface are not a reliable gauge of the bulk volatile content of Mercury. Mercury is the most reduced of the terrestrial planets, so it is uncertain how low oxygen fugacity conditions (-6.3 to -2.6 Δ IW) may affect the partitioning of incompatible elements, such as U and Th [2]. If typically lithophile U and Th partition more into metallic phases under highly reduced conditions, U and Th will be sequestered in the core rather than incorporated into the crust. Bouhifd et al., for instance, performed experiments which showed that $D_{U}^{metal/silicate}$ increases with increased S content and more reducing conditions [3]. Thus, the surface will be depleted in U and Th, and the MESSENGER spacecraft's Gamma Ray Spectrometer data is not representative of Mercury as a whole. The resulting surface ratios would be higher than those of bulk Mercury, suggesting a much more volatile rich environment [2].

This abstract presents experimentally determined metal/silicate partition coefficients of U, Th, and K under reducing conditions of -3.26 to -1.78 Δ IW and different temperatures, in order to constrain the bulk concentrations and ratios of these elements within Mercury. The calculated bulk K/Th and K/U ratios will more accurately represent Mercury's volatile content.

Methods: Experiments were conducted in a QuickPress Piston Cylinder apparatus, using BaCO₃ cell assemblies with graphite furnaces, and oxides, carbonates, and metal mixes in a graphite capsule. Two different sample compositions were used, a U-Th sample containing 2 wt% U and 2 wt% Th, and a K-rich sample containing 17 wt% K. Both compositions were similar to that of EH chondrites, as they are compositionally similar to Mercury, although Mercury is even more reduced. Both compositions were heated to different temperature conditions, ranging from 1500°C to 1700°C in 50°C increments, with the exception of one of the U and Th rich samples. All of the experiments were pressurized to 1 GPa. The experiments were heated for 45 minutes to 3.5 hours, depending on the temperature. The samples containing U and Th were polished using methanol, while the samples containing K were polished dry, using Al₂O₃ powder.

The JEOL 8530F Electron Probe Micro Analysis (EPMA) at NASA JSC was used to measure the major and minor element concentrations. Due to concentrations of U and Th below detection limits in the metal phases, the Laser Ablation Inductively Coupled Plasma Mass Spectrometer (LA-ICP-MS) at the University of Houston was also used to analyze the samples containing U and Th. Two standards were used, NIST-610 and NIST-612, both of which are basalts rich in U and Th, allowing for accurate measurements.

Using the measured U and Th concentrations in the metals and silicate melts, partition coefficients were calculated. Using the minimum and maximum partition coefficient, mass balance equations for degrees of partial melting between 3% and 50%, were calculated for U, Th, and K. U and Th are incompatible elements, thus it can be assumed that there is no U and Th within the residual mantle, which allowed us to simplify the mass balance calculations. This equation was used for the bulk Mercury calculations:

$$X_{\text{bulk}} = 0.73X_{\text{sil}}D_X + 0.27MX_{\text{sil}}$$

X_{sil} = average weight percent U or Th on the surface of Mercury, as determined by MESSENGER

D_X = minimum or maximum partition coefficient of U, Th, or K

M = degree of partial melting

Using the bulk mercury calculations, the K/Th and K/U ratios were calculated for each mass balance equation, and were plotted against the crustal percentage of the mantle, along with the range of feasible crustal percentages calculated from Smith et al. [4].

Table 1. Metal/Silicate Partition Coefficients

U-Th Samples	Temp. (°C)	f _{O2} (ΔIW)	S (wt%)	D _U	Unc. D _U	D _{Th}	Unc. D _{Th}	K-rich Samples	Temp. (°C)	f _{O2} (ΔIW)	S (wt%)	D _K	Unc. D _K
904	1500	-3.2	2.08	6.97E-05	—	9.87E-05	—	916	1500	-2.42	1.45	8.70E-04	8.73E-04
907	1550	-2.8	2.31	2.53E-04	2.92E-04	2.06E-04	1.25E-01	919 LT	1550	-2.33	3.71	1.20E-03	6.90E-04
910 LT	1580	-2.65	3.21	1.20E-04	6.00E-05	2.90E-05	1.71E-05	921LT	1600	-1.95	1.65	1.10E-03	1.53E-03
909	1600	-3.26	0.76	4.00E-05	2.52E-05	4.50E-06	3.72E-07	921 HT	1600	-2.3	0.35	1.00E-03	4.05E-04
924 HT	1650	-2.38	1.25	2.40E-05	4.49E-06	—	—	922	1650	-1.78	0.40	2.00E-03	9.20E-04
923	1700	-2.58	0.61	3.10E-05	1.48E-05	1.00E-05	1.64E-07	925	1700	-1.81	0.92	4.90E-04	1.40E-03

Results: The U-Th samples contained primarily metals and silicate melt, with varying amounts of enstatite crystals and sulfides. Some samples also contained a U-Th oxide. A temperature gradient was visible across some samples, demonstrated by a distinct change in texture and amount of melt, as seen in Figure 1. For some of the samples with a temperature gradient, it was possible to measure elemental concentrations in the silicate melt and the metal blebs, where two distinct equilibrium compositions were found within each sample. The compositions vary for the low temperature and high temperature portions of each sample, but are homogenous within the low or high temperature side. We also found that there are higher concentrations of MgO in the high temperature portions of the samples, and among the K-rich and U-Th samples. The K-rich samples were very similar in texture to the U-Th samples, but contained much smaller anhedral enstatite crystals, due to the high concentration of K.

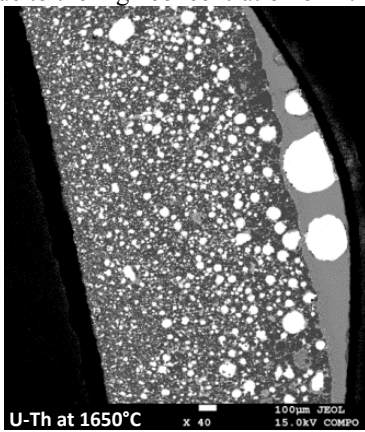


Fig. 1- There is a distinct boundary, representing the liquidus, between the high temperature melt on the right and the lower temperature crystallization, larger metal blebs, and smaller melt percentage on the left-hand portion.

Metal/Silicate partitioning coefficients for each sample are shown, along with temperature, oxygen fugacity, and wt% S in Table 1. The U and Th metal/silicate partition coefficients from the U-Th samples increase with decreasing temperature (See Fig. 2). The $D_{U}^{\text{metal/silicate}}$ values do not show a trend with

oxygen fugacity on their own, but on a larger scale, they follow the trend of increasing $\log(D_{U}^{\text{metal/silicate}})$ with more reducing conditions presented in McCubbin et al. [2]. The trend of Th with respect to oxygen fugacity is unclear, because there are no previous data to improve the range of oxygen fugacities, in order to see the larger scale of the trend. There was no apparent trend for D_U or D_{Th} with respect to S content. D_K remained constant despite changing temperature, oxygen fugacity, or S content.

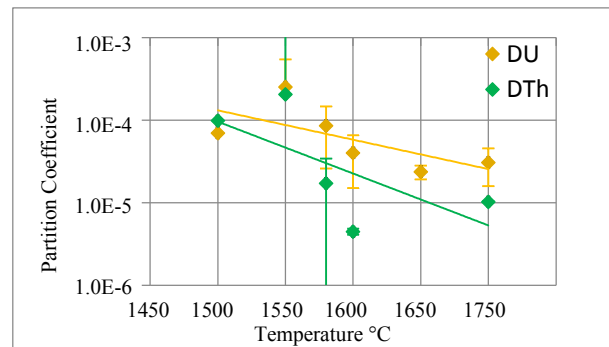


Fig. 2 – D_{Th} and D_U both increase with decreasing temperature.

The maximum and minimum partition coefficients, calculated from the experiments, yield bulk Mercury K/Th and K/U ratios greater than the average surface K/Th and K/U ratios, as displayed in Fig. 3. The bulk K/U and K/Th ratios for Mercury are nearly the same as the surface ratios, suggesting that, within the constraints of these experiments, there is not significant partitioning of U and Th into the core.

Discussion: Oxygen fugacity appears to have the greatest effect on partitioning coefficients of U and Th, because Mercury's interior has such reducing conditions. Our experiments were sub solidus below 1650°C, and mantle-core segregation likely took place between two liquids. Therefore, the trends of increasing Th and U partitioning with decreasing temperature, likely below 1500°C, is not the favored mechanism for U and Th partitioning into the core.

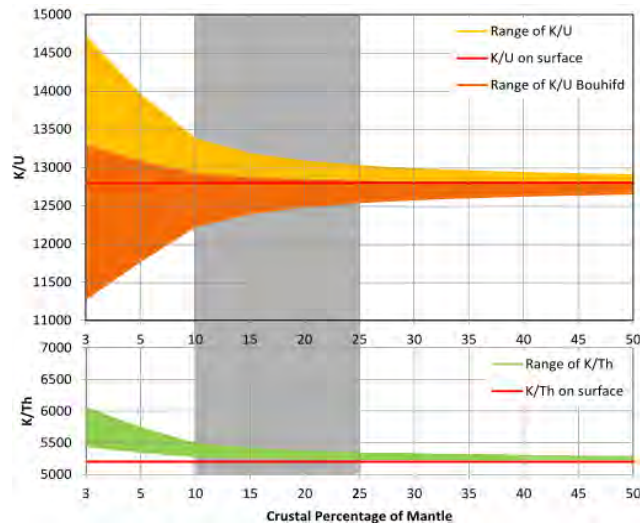


Fig. 3 – Diagram showing bulk K/U and K/Th ratios determined by mass balance calculations, compared to the ratios of the surface. The K/U minimum derived from Bouhifd et al. is in the dark orange [3]. The grey box represents the crustal percentage of the mass of the mantle, converted from depths in Smith et al. [4].

As for the bulk K/Th and K/U of Mercury, the partition coefficients from these experiments are not sufficiently high to shift the range of K/Th and K/U ratios down enough to suggest that U and Th are being partitioned into the core. However, data from Bouhifd et al., increases the maximum partition coefficient of U enough to shift the modeled bulk K/U below the surface ratio. Bouhifd et al. produced experiments on compositions similar to CI chondrites, at different oxygen fugacity conditions, and found a correlation between more reducing conditions and higher $D_{U}^{\text{metal/silicate}}$ values, stating that at $-4.42 \Delta IW$, the D_U was 3.7×10^{-3} [3]. Further experiments for U and Th partitioning with different oxygen fugacity conditions are required to understand the actual bulk K/Th and K/U range of Mercury, but it appears as though only one order of magnitude greater is required for the partition coefficients to be sufficient for U and Th partitioning into the core. While an increase in the U and Th partition coefficients is important for decreasing bulk K/U and K/Th ratios, it is also vital for the $D_K^{\text{metal/silicate}}$ values to remain constant despite temperature or other changes. If the partition coefficient for K were to increase as well, the effect would overshadow the U and Th partition coefficients, and the bulk K/Th and K/U ratios would remain higher than the ratios on the surface. Previous experiments show that increased S will raise the $D_K^{\text{metal/silicate}}$ partition coefficients [5,6]. Although there was no trend between the S content and the U, Th, or K partition coefficients in our experiments, it is possible that our S range was too small to identify the trend. Thus, S content could be an additional variable in the bulk K/U and K/Th ratios. Alternatively, the reverse could be beneficial for dropping the bulk ratios below that of the surface. Bouhifd et al. compiled and added to data concluding that $D_K^{\text{metal/silicate}}$ increase with increasing temperature [6,7,8,9,10,11,12,13].

Summary and Conclusions: This study determined a trend of increasing $D_U^{\text{metal/silicate}}$ and $D_{Th}^{\text{metal/silicate}}$ with decreasing temperature, but ruled this out as a primary mechanism for segregation of U and Th into the core based on temperature of mantle-core segregation. The trend of increasing $D_U^{\text{metal/silicate}}$ and $D_{Th}^{\text{metal/silicate}}$ with more reducing conditions is a much more likely mechanism for partitioning of U and Th into the core, as modeled by partitioning coefficients from Bouhifd et al. [3]. The model shows that a D_U of 3.7×10^{-3} , a result of $-4.42 \Delta IW$, is sufficient for shifting the bulk K/U and K/Th ratios of Mercury below those of the surface. Additional U-Th experiments at more negative oxygen fugacities, between -6.3 to $-2.6 \Delta IW$, should be done in order to provide a more reliable trend of U partitioning and to determine if there is a similar trend with Th partitioning. These experiments could also be used to look at the effects of S content on a larger scale.

Acknowledgements: Thanks to Jennifer Rapp and Kellye Pando for their aid with the Piston Cylinder Apparatus, and to Daniel Kent Ross for guiding us through the use of the EPMA. Thanks to Minako Righter and Rasmus Andreasen at the University of Houston for their help with the LA-ICP-MS.

References:

- [1] Albarède et al. (2009) *Nature* 461(8477) 1227-1233. [2] McCubbin et al. (2012) *Geophysical Research Letters* 39, L09202. [3] Bouhifd et al. (2013) *Geochimica et Cosmochimica Acta* 114, 13-28. [4] Smith et al. (2012) *Science* 336, 214. [5] Chabot and Drake (1999) *Earth and Planetary Science Letters* 172, 323-335. [6] Bouhifd et al. (2007) *Physics of the Earth and Planetary Interiors* 160, 22-33. [7] Oversby and Ringwood (1973) *Earth and Planetary Science Letters* 18, 151-152. [8] Murthy et al. (2003) *Nature* 423, 163-165. [9] Gessmann and Wood (2002) *Earth and Planetary Science Letters* 200, 63-78. [10] Ohtani et al. (1992) *High Pressure Research: Application to Earth and Planetary Sciences*, 341-349. [11] Ohtani and Yurimoto (1996) *Geophysical Research Letters* 23, L01469. [12] Ito et al. (1993) *Geophysical Research Letters* 20, L01538. [13] Hirao et al. (2006) *Geophysical Research Letters* 33, L083.

A Mineralogic and Petrographic Investigation of Unique Foreign Clasts in 3 Ordinary Chondrite Samples.

Jessica M. Johnson¹, Michael E. Zolensky², Queenie Chan², David A. Kring³, ¹Department of Geological Sciences, Central Connecticut State University (1615 Stanley Street, New Britain CT 06050, USA), johnsonj@my.ccsu.edu, ²NASA Johnson Space Center (2010 NASA Parkway, Houston, TX 77058, USA), ³Lunar and Planetary Institute (3600 Bay Area Boulevard, Houston TX 77058, USA).

Introduction: Understanding the processes that forged our solar system is something that has long been desired. Meteorites contain some of the oldest material in the solar system; they can provide us with valuable insights into the conditions of the early solar system. Collisions often occur in our solar system that can result in materials accreting to other bodies as foreign clasts. These foreign pieces may have multiple origins that can sometimes be easily identified as a particular type of meteorite. It is important to interpret the origins of these clasts in an attempt to understand dynamics of the solar system and large movements throughout its early history. There is one such model, the Nice Model, which proposes a reordering of planetary orbits that is hypothesized to have triggered the Late Heavy Bombardment. Clasts found within meteorites that come from objects in the solar system not commonly associated as an impactor could be indicative of such an event suggested by the Nice Model.

The goal of this investigation was to examine foreign clasts enclosed in meteorites. Due to time constraints, only three samples (NWA6169, NWA8330, and NWA6925) that proved to be of particular interest were analyzed in the most detail and will be the primary discussion of this paper.

Methods: An initial analysis of mineralogy was conducted on each whole rock sample using Raman spectroscopy. The laser was calibrated to a silica standard at a wavelength of 514nm. Each sample was analyzed in twelve different regions; six points taken within the clast and six in the surrounding host chondrite. The spectra were analyzed with Crystal Sleuth which allowed the raw spectra to be compared to spectra of known minerals. These points provided a primitive understanding of the mineralogy of the samples before SEM and microprobe analyses were conducted. The samples were then cut to include the clast and the host meteorite material using JSC's diamond blade rock saw. These cut samples were then used to create epoxy thick sections and polished accordingly. The samples were observed using a JEOL JSM-7600F Electron Microscope with beam energy of 15 keV and a current of 900pA at NASA Johnson Space Center. Elemental maps were made to include the majority of the clast and a portion of the host meteorite. The maps were made to help observe any elemental migration between the surrounding host and the clast as well as any such migration within the clast itself. Microprobe analyses were carried out on the JXA-8530F Field Emission

Electron Probe Microanalyzer on the three clasts. The data were analyzed primarily for compositions of olivine, pyroxene, plagioclase, and any metals or sulfides present. The molar compositions were then calculated and plotted on ternary diagrams.

Results: Sample NWA6169 is an unclassified ordinary chondrite from Northwest Africa. Based on petrographic observation of weathering, shock, olivine and pyroxene compositions, and the texture of the chondrules, it falls into the type L3.3 classification. The clast is not similar to the remaining host meteorite. In hand sample it has an aphanitic texture with no distinguishable crystals. The sample resembles an igneous or shock-produced melt that has areas that lack strong euhedral crystalline structure. SEM backscatter imaging showed that many of the minerals remain anhedral with a few exceptions, (Figure 1).

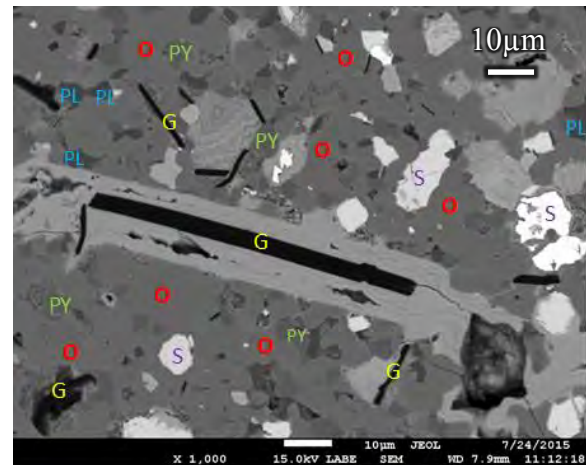


Figure 1: BSE image of a larger graphite crystal within a vein. The surrounding matrix is comprised of olivine (O), pyroxene (PY), plagioclase (PL) and Fe-Ni sulfides (S). Euhedral graphite crystals are present as well as those that have been weathered.

There are small patches of plagioclase-rich material that have no well-defined crystalline structure. There are large euhedral to subeuhedral graphite crystals as well as some that appear fibrous, similar to graphite described in a Krymka meteorite clast by Semenenko & Girich [1]. Some graphite crystals have been replaced by sulfides. The overall modal composition of the clast is 45% olivine, 30% pyroxene, 15% Fe-Ni sulfides (pyrrhotite or troilite), 5% plagioclase, 5% graphite, and <1% metal. Molar ratios were calculated for the olivine, pyroxene, and plagioclase, (Table 1).

Table 1: Molar values of mineral compositions based on the analyzed microprobe data.

	NWA8330		NWA6169		NWA6925	
	Average	Range	Average	Range	Average	Range
Fa	30	28-32	33	31-34	40	29-50
En	71	46-77	69	9-75	57	53-67
Ab	53	4-83	60	7-85	36	17-53

The striking features of this clast are the prominent graphite laths that are randomly oriented throughout the clast. Electron Back Scatter Diffraction was done in an attempt to observe their crystalline structure. However the graphite proved to be too deformed and no strong patterns were collected. Figure 2 shows a deformed graphite crystal over a pore space that an attempt to investigate the three dimensional form of the crystals. A similar technique was performed by Semenenko & Girich [1].

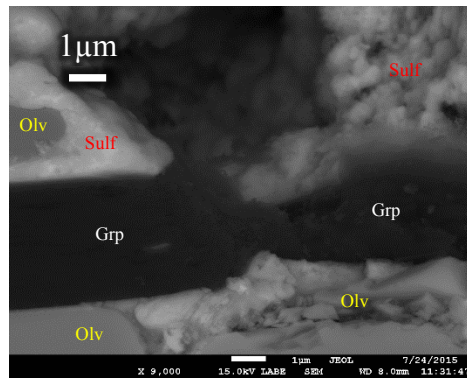


Figure 2: High-magnification BSE of a graphite crystal in NWA6169 that has been partially deformed over a pore space. The overall crystal has an approximated thickness of about 1.5 μm and this crystal is approximately 4 μm across suggesting a thin, lath shape to it.

The next sample reported on in this investigation was NWA8330, another ordinary chondrite that is classified as a type LL3. It contains a clast that is quite similar to NWA6169. It has euhedral to subeuhedral graphite laths as well as being comprised of a similar mineralogy to NWA6169. Some of the clast seems anhedral in texture while having a more euhedral texture in other areas. The olivine and pyroxene crystals are mainly euhedral and the plagioclase appears more as singular crystals or possible melt globules, (Figure 3).

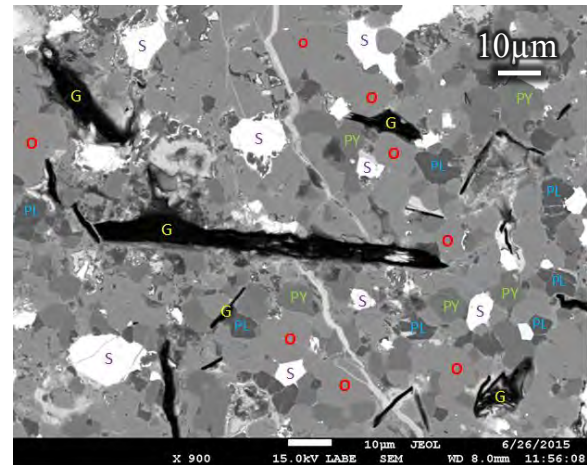


Figure 3: Graphite that has been partially deformed surrounded by a matrix of anhedral olivine (O), pyroxene (PY), plagioclase (PL) and Fe-Ni sulfides (S).

The percentages of the different minerals present in NWA8330 are very similar to that of NWA6169, except there appears to be more sulfides present in NWA8330. The overall modal composition of the clast is 45% olivine, 30% pyroxene, 13% Fe-Ni sulfides (pyrrhotite or troilite), 7% plagioclase, 5% graphite, and <1% metal. Molar ratios were then calculated using the same methodology for olivine, pyroxene, and plagioclase, (Table 1). NWA8330 presents itself overall as being more aphanitic with more isolated pockets of plagioclase that appears to be primarily poikilitic with either spherical nodules of possibly glassy material or of remelted olivine. The spherical nodules were too small to permit a decent composition by microprobe analysis.

The final sample examined in this study was NWA6925. NWA6925 is classified as a L3.15 ordinary chondrite. It contains a rather large clast that is different from NWA6169 or NWA8330. The clast is mainly composed of olivine and pyroxene with areas of dehydrated phyllosilicates. These dehydrated phyllosilicates are seen both as long veins and also within pockets of apparently partially altered pyroxene. The bulk texture of the sample is granular rather than crystalline. The sample is composed of 50% olivine, 40% pyroxene, 5% plagioclase, and 5% Fe-Ni sulfides. Molar values are listed in table 1. The veins are very fine-grained and in some portions have an oriented pattern suggesting dehydration, (Figure 4). Most of the “dehydrated” phyllosilicates now olivines and pyroxenes. Some pyroxenes were found with a poikilitic texture as they had begun altering.

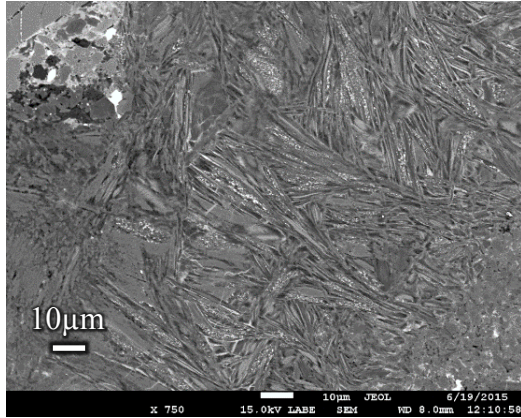
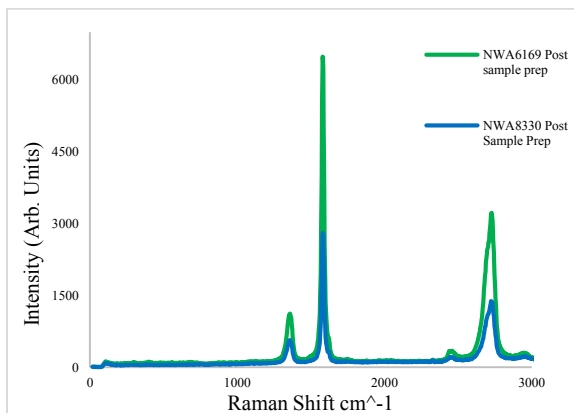


Figure 4: BSE image of one of the dehydrated phyllosilicate pockets. They are now olivine and pyroxene.

Discussion: All three samples tell their own story. NWA6169 and NWA8330 are similar in appearance and composition, yet NWA8330 has been more deformed. The relationships of these two samples are still unknown, yet they do resemble a clast found in Krymka by Semenenko & Girich [1] in 1995. The average compositions of olivine and pyroxene reported by Semenenko & Girich [1] were $\text{Fa}_{28.8-35.0}$ and $\text{En}_{44.5-77.3}$. These are similar ranges to the compositions found in both NWA6169 and NWA8330, (Table 1). Semenenko & Girich [1] proposed that the clasts were most likely melt produced clasts from a fairly large impact. The graphite present in NWA6169 and NWA8330 had to have formed at a very high temperature to have the observed texture. Raman spectral data of the graphite peak, (Chart 1), suggests a relatively high temperature cooling gradient as noted in Beyssac & Lazzeri [2] and Fries & Steele [3]. Semenenko & Girich [1] suggested that the graphite in the Krymka clast formed from a melt rather than a gas due to its preserved structure. Raman spectroscopy also suggests that the graphites are of similar structure in NWA6169 and NWA8330.

Chart 1: Raman Spectra of graphite NWA8330 and NWA6169.



The comparison of the crystal boundaries and preservation between NWA6169, NWA8330, and the unique Krymka clast indicates these samples could be related. The process that formed all three of the clasts is still unknown; however one such possibility is the proto-earth/moon collision. Bottke et al. [4] proposed the possibility that pieces from this collision have the potential to have been deposited in the asteroid belt after being ejected from the initial collision. Unfortunately Bottke et al. [4] did not suggest a way to test a sample for this - however it is something that will be pursued of in future work. Considering that the clasts contain plagioclase, they could be dated to reveal their ages of crystallization. Acquiring ^{18}O isotope ratios of the clasts and comparing them to the Earth's ratios could be useful in supporting or eliminating the possibility of such an origin. One other possibility of formation of these clasts is a C type asteroid which underwent extreme melting and recrystallization, but the amount of carbon needed for that is uncertain. There is little in the literature of such an impact occurring or what a melt from an impact to that degree would recrystallize into. Semenenko & Girich [1] noted that few graphite crystals similar to those in the Krymka clast are known, so perhaps this is not the explanation.

NWA6925 is most likely an ordinary chondrite that had been altered in a very aqueous environment while still within its parent body. The dehydration stage could have occurred after it was ejected from its parent body and collided with the ordinary chondrite it is a part of now, or before this on some other part of the same asteroid – the data permit no firm conclusion. The phyllosilicates underwent a dehydration process and transformed into olivine and pyroxene. All three samples investigated in this study have proved to have very interesting and unique origins all worth studying in the future.

Acknowledgments: I would like to thank those individuals who helped me along the way; Loan Le, Kent Ross, and Eve Berger for helping me out in the SEM and Microprobe laboratories. James Martinez for attempting to gather EBSD data on the graphite laths. Most of all, Michael Zolensky, Queenie Chan, and David Kring for giving me the opportunity to work with them. I have gained a plethora of knowledge and I could not be more grateful.

References: [1] Semenenko V.P. and Girich A.L. (1995) *Mineralogical Mag*, 59, 443-454. [2] Beyssac O. and Lazzeri M. (2012) *EMU notes in Min.*, 12, 415-454. [3] Fries M. and Steele A. (2011) *Springer Series in Optical Sciences*, 158, 111-135. [4] Bottke W.F. et al. (2015) *Science*, 348, 321-323.

RARE EARTH ELEMENT PARTITIONING IN LUNAR MINERALS: AN EXPERIMENTAL STUDY.

E. C. McIntosh¹, J.F. Rapp² and D. S. Draper³, ¹University of South Carolina, Columbia, SC, 29208..., ²Jacobs, NASA Johnson Space Center, Houston, TX 77058, ³NASA Johnson Space Center, Houston, TX 77058.

Introduction: Trace element partitioning between olivine and melt in lunar compositions has not been widely studied because it has been assumed that the olivine/melt partition coefficient is so low that it is negligible, based on terrestrial data [1]. This abstract presents results from high-pressure and -temperature experiments at low oxygen fugacity investigating rare earth element (REE) partitioning between olivine and melt in a composition relevant to lunar magmatism.

The current hypothesis for lunar formation is that the Moon differentiated in a global scale event resulting from the crystallization of a lunar magma ocean (LMO). Negative europium anomalies are ubiquitous in lunar basalts and volcanic glasses, and indicate large scale plagioclase removal from the lunar mantle, and therefore evidence for the differentiation of the LMO [2, 9].

REEs are also useful in interpreting the composition of the lunar interior. It is common for lunar basalts and volcanic glasses to be depleted in light REEs (LREE), and more enriched in heavy REEs (HREE) [2]. The partition coefficient (D) is the ratio of the concentration of a trace element in the mineral to the concentration in coexisting equilibrium liquid. REEs are highly incompatible in olivine (i.e. $D \ll 1$), but even the small amounts of REE that can be stored in olivine, which could affect the trace element budget of the Moon. [3-6]

The starting composition for this study was based on lunar sample 14307, [7] and mimics A14B used by [3]. Currently no lunar samples have been identified as mantle rocks, but A14B is based on the most ultramafic green glass sample, and has therefore likely undergone the least modification from its initial primary mantle melt.

Methods: The starting composition was synthesized from mechanical mixtures of anhydrous oxides and carbonates, with 200ppm of each trace element added using ICP-MS standard solutions after decarbonation at 800°C. The mixture was then melted at 1600°C, and resultant glass re-ground for 30 minutes to ensure homogenization, before conditioning at 1 log unit below the iron-wustite (IW-1) buffer at 1000°C for 24 hours.

16 experiments have been completed. 11 experiments from 0.5 GPa to 1.5 GPa and 1450°C to 1650°C were performed in a 13mm QuickPress piston cylinder and 5 experiments at 3.5 GPa to 4.0 GPa were performed in a multi-anvil press. Graphite capsules were used in both assemblies. Piston-cylinder assemblies used BaCO₃ as a pressure medium and graphite heaters.

Multi-anvil assemblies used rhenium heaters. Isobaric quench was carried out in all experiments by cutting power to the heater while maintaining pressure.

Experimental run products were mounted in epoxy, ground, polished, carbon coated, and analyzed for major and minor elements using the JEOL 8530F electron microprobe at NASA Johnson Space Center. For trace elements, the run products were then analyzed using Laser Ablation Inductively Coupled Mass Spectrometry (LA-ICP-MS) at the University of Houston using USGS glasses BHVO and BIR as standards.

Results: 16 successful experiments are discussed here. A summary of run products can be found in Table 1. At 0.5 – 1.5 GPa, olivine is the liquidus phase (Fig. 1), with orthopyroxene (opx) co-crystallizing with olivine at temperatures below 1550°C. The liquidus at 0.5 GPa is approximately at 1600°C, rising to 1650 °C by 1.8 GPa. At 3.5. GPa, however, it appears to be depressed, although there is major uncertainty in the temperatures of the high pressure experiments due to the thermal gradient across the capsule and a slight offset between sample and thermocouple. Thermal modelling of the experimental assembly shows that the hotspot in the capsule could be more than 100°C hotter than the temperature measure by the thermocouple at the top of the capsule.

The forsterite content of experimental olivines ranged from Fo₈₁ in near-liquidus experiments (e.g. Fig. 1) down to Fo₇₆ in equilibrium with opx. Orthopyroxene compositions show a similar trend, ranging from enstatite-rich (En₈₁Fs₁₅Wo₄) in near liquidus experiments at high pressure to more pigeonitic (En₆₈Fs₁₉Wo₁₂) at low pressure co-crystallizing with olivine.

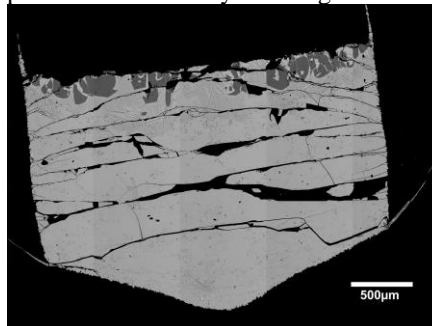


Figure 1: An example of a typical near-liquidus piston-cylinder run product (CM8). Crystals are olivine.

Runs CM-8, CM-10, CM-12, and CM-16 contained crystals that were suitable to analyze using LA-ICP-MS to determine partition coefficients.

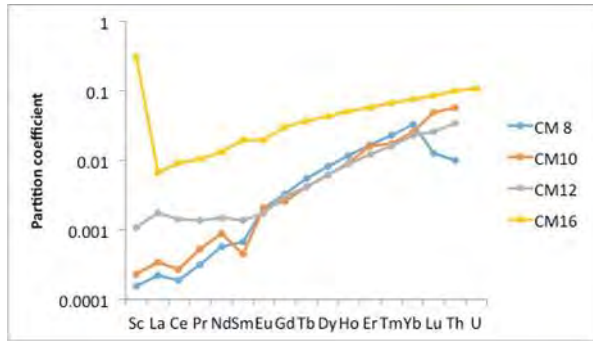


Figure 2: Plot of experimentally determined partition coefficients. $D_{\text{REE}}^{\text{olivine/melt}}$ were obtained from experiments CM 8, CM10, and CM 12. $D_{\text{REE}}^{\text{opx/melt}}$ is shown for CM16.

Olivine/melt partition coefficients increase from the LREE (La – Gd) to HREE (Y – Lu) with Lu being the most compatible (Fig. 2), although all REE can still be considered very incompatible in olivine. The concentration of LREE such as La and Ce is so low in olivine that it is close to the detection limit of the instrument. Therefore the uncertainty on these measurements is much larger, and the resultant partition coefficients must be considered with some caution. For example the incorporation of a very small melt inclusion will proportionally change the measured LREE much more than the measured HREE. It is likely that we observe this effect in our measurements of CM12, where two olivine analyses (Points 7 and 5, Fig. 3) have much higher

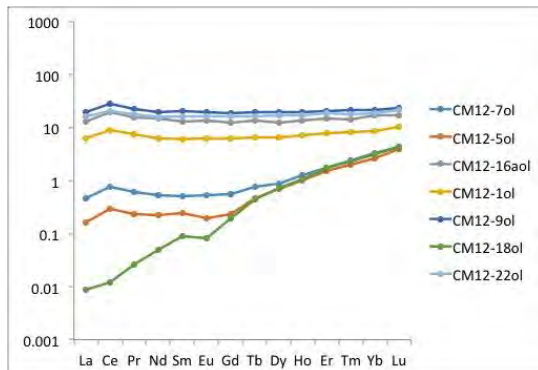


Figure 3: REE abundance (ppm) in olivine analyses of CM12. Crystals may have contained small inclusions that affected the measured LREE abundances, but not the HREE

LREE than the third (point 18, Fig. 3), but mid- to HREE are the same for all analyses. Other points are clearly contaminated with melt (points 1, 9, 16 and 22, Fig. 3), likely by ablating through the crystal during analysis.

Discussion:

Phase Equilibria: Our experiments are offset to higher temperatures than those of [3] by approximately 100°C. There are several potential reasons for this discrepancy, including a difference in temperature

calibrations of piston-cylinder apparatus between the two laboratories (MIT and JSC). Another possibility is that there is a higher concentration of H₂O in their experiments than in ours. Water generally lowers the liquidus temperature and temperature of phase transitions in magmas. One difference in technique between the two studies is in the initial preparation of starting material, in that our composition was glassed and reground before conditioning at IW-1, whereas no melting step is described in [3]. It is possible that this step is important in removing adsorbed H₂O from the starting material and ensuring a truly dry melt.

Trace Element Partitioning: Our experimentally determined partition coefficients can be used in a variety of petrologic calculations, for example, in calculating the REE composition of mare basalt source regions, and tracking the trace element budget of LMO crystallization. Using our experimentally determined $D_{\text{REE}}^{\text{olivine/melt}}$ we can calculate the abundance of REEs in the lunar interior at increasing degrees of fractional crystallization using the Rayleigh fractionation equation (after [6]). When beginning from a chondritic source composition [10], after 50% olivine crystallization REE abundances in the residual melt increase by approximately a factor of 30, as REE are very incompatible in olivine. However, our new partition coefficients suggest that olivine also has the potential to fractionate LREE from HREE (Fig. 5). Sm/Yb increases from chondritic 0.905 to 0.959 after 50% olivine fractionation crystallization as HREE such as Yb are slightly more compatible in olivine than LREE such as Sm, leading to an enrichment of LREE relative to HREE in the melt. This distribution is opposite to that observed in lunar basalts, which are enriched in HREE relative to LREE [2].

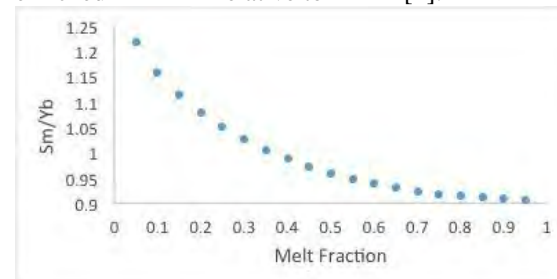


Figure 5: Sm/Yb evolution during fractional crystallization. Sm/Yb increases as fractional crystallization increases (melt fraction decreases), as Yb is more compatible in olivine than Sm.

Our experimentally determined partition coefficients can also be used to model crystal composition in lunar cumulates. For example, when starting from a chondritic composition [10], crystallizing olivine will have a negative Eu anomaly (Fig. 6). Negative Eu anomalies in lunar basalts are generally assumed to be

the result of plagioclase extraction from the mantle during LMO crystallization (e.g.[2]), however our new olivine/melt D_{REE} suggest that there is the potential for the lunar mantle to have an inherent negative Eu anomaly that is not related to formation of a plagioclase-rich flotation crust. This however bears further examination, as REE abundances in olivine are very low, and it is not yet clear whether this could have wider implications for the composition of the LMO cumulates and lunar basalt sources.

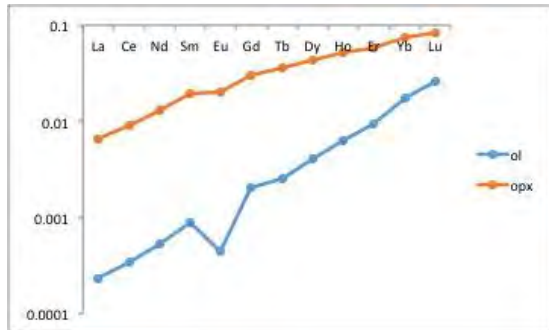


Figure 6: Chondrite normalized REE abundances in modelled olivine (blue) and opx (orange). Experimental D_{REE} produce olivine with a marked negative Eu anomaly.

Conclusions and future work: The interior of the Moon likely contains a large amount of olivine, therefore olivine/melt D_{REE} are useful in interpreting the composition of the lunar mantle. Using new experimentally determined olivine/melt D_{REE} we can begin to understand the trace element composition of the lunar

mantle, and the petrogenesis of lunar magmas. Our new D_{REE} allow LREE to be enriched in the residual melt during olivine crystallization, and crystallizing olivine to have inherent negative Eu anomalies, adding further to the debate on LMO crystallization processes. Future work will involve expanding this study to a larger suite of trace elements by carrying out lattice strain modeling. Further experiments will also allow for determination of the olivine-opx MSP between 2-2.5 GPa, and investigate the cause of the seemingly depressed liquidus at 3.5-4 GPa. One explanation for this is an opx-garnet MSP at higher pressure, as shown by [7] on an Apollo 15 green glass composition similar to the one discussed here. Further examination of the run products is possible using FTIR analysis to determine the water content of the experiments to determine if this is a likely cause of the variation between our experiments and those of [5].

References: [1] Bédard J.H. (2005) *Lithos*, 64, 5919-5934. [2] Shearer C.K., et al (2006) in *RiM New Views of the Moon*, 60, 365-518. [3] Elkins L.T., et al. (2000) *GCA*, 64, 2339-2350. [4] Elkins-Tanton L.T. et al. (2011) *EPSL*, 304, 326-336. [5] Longhi J. (2006) *GCA*, 70, 5919-5934. [6] Snyder G.A. (1992) *GCA* 56, 3809-3823. [7] J.W. Delano. (1986). *Journal of Geophysical Research*, 91, 201-213.[8] Draper D.S., et al. (2006) *GCA*, 70, 2400-2416. [9] Elardo S.M., et al. (2011), *GCA*, 75, 3024-3045. [10] Anders & Grevesse (1989) *GCA* 53 (1), 197 – 214.

Run #	P (GPa)	T (°C)	Duration (hours)	Phase Assemblage	Modal Proportions	Σr ²
CM10	0.5	1550	2	gl,ol	94:5	0.95
CM 17	0.5	1600	1.5	gl	100	-
CM 14	0.5	1650	1.5	gl	100	-
CM 2	1	1450	6	gl, ol, opx	-	-
CM 19	1	1550	3	gl, ol	85:15	0.10
CM 8	1	1600	4	gl, ol	86:14	0.27
CM 9	1	1650	2	gl, ol	-	-
CM 1	1.5	1550	3	gl, ol, opx	80:16:4	0.06
CM 12	1.5	1600	1.5	gl, ol	90:10	0.08
CM 13	1.5	1650	1.5	gl	100	-
CM 19	1.8	1600	1.5	gl, ol	84:15	0.10
CM 15	3.5	1500	2	gl, opx	-	-
CM 6	3.5	1600	4	gl	100	-
CM 16	4	1500	2	gl, opx	84:16	0.15
CM 18	4	1550	2	gl, opx	90:10	0.13
CM 7	4	1600	1	gl	-	-

Table 1: Conditions and results of experiments. P= pressure, T=temperature, r²=value of the least squares mass balance calculation used to determine modal proportions

PETROLOGY, BULK COMPOSITION, AND PROVENANCE OF METEORITE NWA5000 A. B. Nagurney^{1,2}, A. H. Treiman², P. D. Spudis², ¹Department of Geology and Environmental Geosciences, Lafayette College, Easton, PA 18042 (nagurnea@lafayette.edu) ²Lunar and Planetary Institute, Houston, TX 77058

Introduction: Lunar meteorites provide information about the composition of the Moon that cannot be inferred from Apollo samples or remote sensing data. Lunar meteorite Northwest Africa 5000 (NWA5000) was discovered in 2007 in Morocco (Fig. 1a) and at 11.5 kg is the second largest known lunar meteorite [1]. Previous work has looked at the petrology and diffusion of metals within NWA5000 [1,2], but this is the first comprehensive study of the meteorite.

NWA5000 is a polymict leucogabbro breccia, with light-toned rock fragments set in a dark fragmental matrix. It is different from other known lunar meteorites because both the matrix and clasts contain very high concentrations (~2%) of metal [2]. Other lunar samples contain small proportions of metal [e.g., 3], mostly of meteoritic origin, but not at the proportion seen in NWA5000. NWA5000 is interesting because it may have an unusual parent material or be a product of a previously unknown process occurring on the moon.

Sample and Methods: We examined a 0.74 gram slab of NWA5000, which exposes nearly equal parts of clast and matrix material (Fig. 1b). We analyzed the chemical compositions of nine metal grains and their surrounding silicate matrix using a CAMECA SX100 electron microprobe. The metal grains were analyzed using a 15kV, 60nA beam; the silicate grains were analyzed using a 15kV, 10nA focused beam.

To acquire mineral proportions of the clast, we used chemical element maps created on a JEOL 7600F scanning electron microscope to obtain mineral proportions in MultiSpec. Using the chemical compositions determined by our electron microprobe data, we converted the mineral proportions into a bulk chemical composition of the clast.

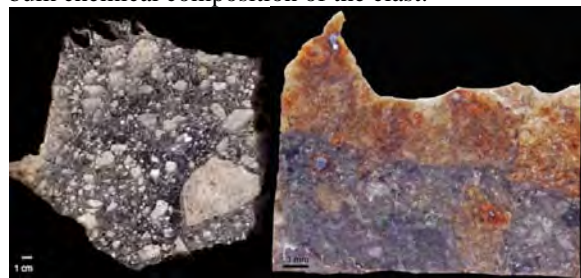


Fig. 1a & 1b. NWA5000. a) Full section through meteorite (photo courtesy of The Hupe Collection) b) Studied slab. Note the leucogabbro clasts and the dark matrix.

We compared the composition of NWA5000 to known lunar samples and chondrites to develop a mixing model for the formation of NWA5000 and then compared the composition of NWA5000 to remote sensing data from the Moon in order to constrain its possible source region and crater.

Results:

Petrography: The mineral composition of the light clast is: 66.6% anorthite, 18.8% augite, 6.8% pigeonite, 5.6% olivine, 1.9% kamacite, and 0.3% merrillite.

The white clast contains six large (0.5-1.0 mm) metal grains. Fig. 2 displays the characteristic texture of the rest of the clast. It has a subophitic texture that is described as ‘melt-rock’ and contains large (>200 μm) anorthite grains. The more calcic plagioclase (An_{96}) is found in only larger (>200 μm) plagioclase fragments in a subophitic matrix of less calcic plagioclase (An_{92}) and subhedral olivine with interstitial augite and pigeonite.

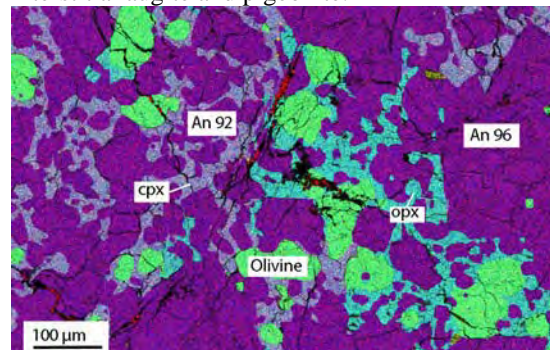


Fig. 2. False color image of impact melt texture and large plagioclase grains. Red=Ca, Blue=Mg, Green=Fe

The matrix around the clast consists of fragments of minerals from the clasts, mineral fragments not related to the clasts, and a variety of fine-grained lithic and vitreous fragments.

The anorthite compositions in the clast range from An_{92} to An_{97} . The average of the least calcic plagioclases is An_{93} and the average of the most calcic plagioclases is An_{96} . The most calcic plagioclase grains are in the ferroan anorthosite field, and the less calcic compositions are in the norite/gabbro-norite field [4].

There are two distinct pyroxene compositions: augite and pigeonite. As seen in Fig. 3, the augite compositions have less variation than the pigeonite compositions.

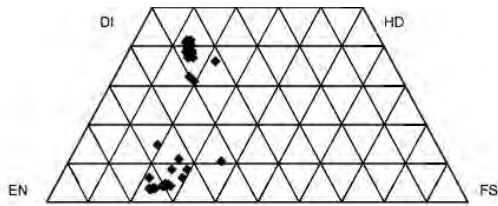


Fig 3. Ortho- and clinopyroxene compositions in the gabbronorite clast.

The average Mg# for olivine is 68.5. The average olivine Fe/Mn ratio is 88, and it ranges between 80-96, which is consistent with lunar material [4]. The metal is kamacite, $\text{Fe}_{92}\text{Ni}_6\text{Co}_{0.5}$, and its Ni/Co in the metal is commensurate with meteoritic metal [5]. Merrillite grains were identified by EDS spectra, but due to time constraints, no microprobe measurements have been taken.

Bulk Composition: Table 1 lists the calculated bulk composition of the leucogabbronorite clast.

Component	Weight Percent
SiO ₂	44.9
TiO ₂	0.4
Al ₂ O ₃	23.0
Cr ₂ O ₃	0.2
FeO	5.2
MnO	0.1
MgO	7.8
CaO	15.5
Na ₂ O	0.4
Fe	1.7
Ni	0.1
Co	0.01

Table 1: Chemical composition of the white gabbronorite clast.

Discussion: This section will review the evidence for the lunar origin of NWA5000, then discuss the formation of NWA5000 as can be discerned from the clast itself, and finally move on to discussing NWA5000 in context of large scale lunar geologic processes.

Evidence for Lunar Origin: Despite the high concentration of metal in NWA5000, there is considerable evidence that the meteorite is of lunar origin. Oxygen isotopes fall along the terrestrial fractionation line [1]. The Fe/Mn ratio and Mg# of olivine are in line with Apollo samples and other lunar meteorites [4]. NWA5000 is high in CaO

(~16%), which is another indication of its lunar provenance [4].

Evidence for Slow Cooling of the Clast: The clast exhibits the texture of an impact melt (Fig. 2). Throughout the clast, pyroxene grains surround olivine grains. Some metal grains show signs of nickel and cobalt diffusing from the metal into either the matrix or the clast, suggesting that metal equilibrated with the lunar rock. Gallium diffused from metal in the matrix into a large anorthosite grain [2]. Both the orthopyroxene and clinopyroxene grains have a nearly homogenous composition and based on the distribution their compositions, the pyroxene grains in the clast most likely cooled at 1100-1200°C [6]. Thus, the white clast in NWA5000 most likely cooled slowly and remained at a high temperature for an extended period of time.

The clast contains a range of anorthite compositions. The most calcic anorthites (An₉₆) are larger clasts that likely represent refractory, unmelted highlands material. The less calcic anorthites are found within the impact melt texture, which suggests that they crystallized as part of an impact melt sheet after the impactor hit the surface.

Analysis of Silicate-Chondrite Mixing: To assess the nature of the parent material for NWA5000, we created a mixing model to determine if compositions of known chondrites and lunar rocks could be mixed together in a specific proportion to create NWA5000. Our models put an upper limit on the amount of silicate from the chondrite that could be present in NWA5000. These models show that for the silicate composition of the clast, if the parent meteorite is an H chondrite, no more than 25% of the silicate minerals could have come from the impactor. If the parent meteorite is an L or LL chondrite, no more than 30% of the silicate minerals could have come from the impactor, and if the parent meteorite was an EH chondrite, then no more than 40% of the silicate minerals could have come from it.

The model results are not consistent with the amount of metal present in NWA5000. LL chondrites contain 3-5% weight percent metal, so close to 100% of the metal from the original chondrite metal would be transferred into NWA5000 because NWA5000 is roughly 2% chondrite metal. Thus, if the impactor was chondritic, the metal from that body would have to concentrate in the impact melt sheet, possibly through some type of differentiation process [e.g. 7]. Mixing models also indicate that pure ferroan anorthosite (e.g. sample 154150) is too poor in ferromagnesian elements to be the lunar parent of NWA5000 [4].

The siderophile element profile of the metal grains does not match the siderophile element profile of any known chondrite or iron meteorite [2].

Because NWA5000 is metal rich, in order to preserve the metal from the original impactor, the original impact was probably at low velocity and did not result in the complete vaporization of the impactor.

Age Data for NWA5000: Calculated ^{40}Ar - ^{39}Ar ages of NWA5000 indicate (for the initial 70% of ^{39}Ar released) an impact at about 500 Ma that most likely exposed the sample to the lunar surface. The following ~30% of ^{39}Ar release is consistent with a 3.2 ± 0.1 Ga age date, which could potentially be the age the event that created the initial gabbro impact melt sheet [8].

Exposure ages (^{10}Be , ^{14}C , ^{36}Cl , cosmogenic ^{21}Ne) support the following exposure history of NWA5000: after spending about 600 Ma in the lunar regolith, the meteorite experienced a relatively short transition time from the lunar surface to the earth's surface (1.3 kyr) where its terrestrial age is potentially as short as 1000 years, with an upper limit of 10.4 Ka [9].

Provenance: NWA5000 is richer in clinopyroxene (~19%) than most of the recovered lunar samples and meteorites [10]. Based on spectral reflectance data from Kaguya, high calcium pyroxenes (HCP; clinopyroxene) can be found throughout the lunar highlands, particularly within some fresh impact craters [11]. NWA5000 exhibits a low Ti-high Fe (highlands) trend, which is consistent with the more mafic areas of the lunar highlands indicating that the lunar provenance of NWA5000 is most likely a relatively mafic area of the lunar highlands (e.g., gabbro). Candidate areas include the floor of the Lomonosov-Fleming and South Pole-Aitken basins, the near side of the southern highlands, and the King crater vicinity [12].

Combining the mineralogical data from Kaguya [11] and the chemical information from Clementine [12], we have identified several fresh craters that possess compositions similar to that of NWA5000. Exposure ages suggest creation of the rock in an impact event more recent than 600 Ma. In comparing these data, we suggest that NWA5000 could have come from one of the following Copernican-aged craters: Bürg, Faraday C, Glushko, King, Necho, Robertson, Rutherford, Thebit A, or Tycho.

Conclusion: Based on this study and previous work [1,2], NWA5000 can be classified as a metal-rich, polymict leucogabbro. It most likely formed through series of impacts. The initial impact was probably the collision of a large metal rich asteroid that crashed into a mafic area of the lunar highlands. This impactor was traveling at a low enough velocity so as to not completely vaporize the projectile. Instead, it was mixed into and incorporated as part of the impact melt that slowly started to cool. The metal started to equilibrate with the silicates in the

surrounding impact melt sheet and eventually, the melt sheet cooled into the leucogabbro.

At some point later in the Moon's history, another impactor collided with this melt deposit. Since the matrix shows no evidence of impact melting, this later impact was probably of smaller magnitude. It did not result in any large-scale impact melting on the moon, but it did break up the previous impact melt sheet and brecciate it. The quenched texture and broken up nature of fragments in the matrix in NWA5000 indicates that the matrix cooled relatively quickly after this impact.

The resulting breccia resided near the lunar surface for the last 600 Ma before being ejected from the Moon and transferred to the Earth about 1000 years ago where it resided in the African desert prior to discovery. The complexity and unique characteristics of NWA5000 suggest that additional work on its composition and history may provide additional insight into lunar processes and evolution.

References: [1] Irving, A.J., *et al.* (2008) *LPSC XXXIX*, 2168 [2] Humayun, M. & Irving, A.J. (2008) *Goldschmidt Conference Abstracts* A402 [3] Warren P.H. *et al.* (1987) *JGR* 92, E303 [4] Jolliff, B. L., *et al.* (2006) *New Views of the Moon*, 95, 103 [5] Wittman, A. & Korotev, R.L. (2013) *LPSC XLIV*, 3035 [6] Lindsley, D.H. (1982) *American Mineralogist* 68, 484-485 [7] Grieve R.A.F. *et al.* (1992) *JGR* 92, 14113 [8] Fernandes, V.A. (2009) *Goldschmidt Conference Abstracts* A365 [9] Nishiizumi, K., *et al.* (2009) *LPSC XL*, 1476-1477 [10] Korotev R. (2005) *Chemie der Erde* 65, 297 [11] Yamamoto S. *et al.* (2015) *JGR* 120, 831-848 [12] Spudis, P.D., *et al.* (2002) *LPSC XXXIII*, 1104

LL-CHONDRITE DOM-10092: A SHOCK-METAMORPHOSED SAMPLE FROM AN IMPACT-MODIFIED ASTEROID. P. R. Phelps¹ and D. A. Kring², ¹Depts. of Geosciences and Physics, University of Tulsa, 800 S. Tucker Dr., Tulsa, OK 74104, patrick-phelps@utulsa.edu. ²Lunar and Planetary Institute, 3600 Bay Area Blvd. Houston, TX 77058.

Introduction: Meteoritic samples of asteroids record a collisional record from the time of planetary accretion 4.5 billion years ago to the present day. An interesting subset of those samples are impact melt breccias because they can be used to determine the ages of collisional events, along with peak temperatures and cooling rates, from which the size of the impact event can sometimes be determined. The purpose of this study is to analyze the petrological and chemical properties of the meteorite Dominion Range (DOM) 10092, which was classified as an LL impact melt breccia [1]. We found, however, that this sample is not an impact melt breccia, but rather a cross-cut with zones of much lower temperature cataclastic zones. We suggest a revised classification as an LL chondrite with a type 4 thermal metamorphic overprint and a subsequent stage 3 shock metamorphic overprint.

Analytical Methods: Optical microscopy was used to evaluate the lithologies and minerals within the meteorite. Chemical compositions of minerals were measured with a JEOL 8530F electron microprobe at the Johnson Space Center. Silicate and oxide phases we analyzed with an accelerating voltage of 15 keV, a beam current of 20 nA, and a beam diameter of ~1 μm . Metals and sulfides were analyzed with an accelerating voltage of 15 keV, a beam current of 20 nA, and a beam diameter of ~1 μm (metals) or ~3 μm (sulfides). Some analyses were conducted as linescans with an analytical spacing of 2 μm .

Petrography: DOM 10092,7 has two textural domains: (i) a chondrule-bearing domain that largely preserves the original chondritic texture of the accreted asteroid and (ii) a fragmental domain that is optically dark. This fragmental domain is the region interpreted to be an impact melt in the original classification of the meteorite [1]. A point count (4894 points) indicates the thin-section (81.1 mm^2) is 60.4% domain (i) and 39.6% domain (ii). Fusion crust is also apparent along one edge of the thin-section. The sample is fairly weathered. Most of the sample near the fusion crust is covered with a small amount of hematite, with some hematite veins. Some of the metal/sulfide shock veins that cross-cut the sample have also been altered to hematite. Large metal and sulfide particles are more abundant in the fragmental domain than in the chondrule-bearing domain (twice as many with sizes

greater than 200 μm). However, particles smaller than 80 μm were more abundant in the chondrule-bearing domain (almost 3x as many). Feldspathic minerals are very rare in this sample. They tend to only reside in chondrule mesostasis as microcrystalline aggregates. Most of the feldspathic grains are too small to analyze. Rare chromite was observed.

Chondrule-bearing domain. Chondrules dominate (80.5%) the domain. Intervening areas are affected by hematite alteration, making identification of matrix phases difficult. The chondrules are sharply defined to readily delineated. The average chondrule diameter is ~580 μm , which corresponds to the dimensions seen in other LL chondrites [2]. Olivine and pyroxene within the chondrules tend to be fairly large (on average ~200 μm) and have euhedral to subhedral morphologies. The pyroxene crystals have both structural states: orthorhombic and monoclinic. However, the majority (>80%) are orthorhombic.

Olivine compositions range between Fo₇₀ and Fo₇₅. The overwhelming majority have a composition of Fo₇₂ or Fo₇₃. Pyroxene compositions cover a much wider range. Of the grains analyzed, only a few can be considered high-Ca pyroxenes (greater than 5% Wo content). These grains range from Wo₆₋₃₁En₅₃₋₇₈Fs₁₄₋₂₀. Low-Ca pyroxene compositions range from Wo₀₋₄En₄₉₋₉₆Fs₃₋₄₈. Larger (>15 μm) crystals of pyroxene are zoned. The widest zoning range within one grain had a core of Wo₀En₉₂Fs₇ and a rim of Wo₀En₇₇Fs₂₂. For a complete distribution of both sets of data, see Figure 1. The sulfide is troilite, having a nearly 1:1 ratio of Fe to S. The Ni content is always less than 1 mol%. Large particles of metal suitable for microprobe analyses are rare. Therefore, no analyses were done on metals within this domain. Compositional zoning is evident in backscattered-electron (BSE) images of pyroxene but not olivine. Chondrule mesostases either quenched to a microcrystalline assemblage or the once-glassy mesostases are devitrifying (Figure 2).

Fragmental domain. Olivine and pyroxene compositions are similar to those in the chondrule-bearing domain. Little of the pyroxene is zoned, however, which may be due to fragmentation of zoned grains and/or diffusional equilibration of the smaller (<15 μm) crystal fragments. Only the fragments >15 μm show zoning. Troilite and metal are both present and the latter are larger in this domain than the other domain. The metallic minerals are taenite and

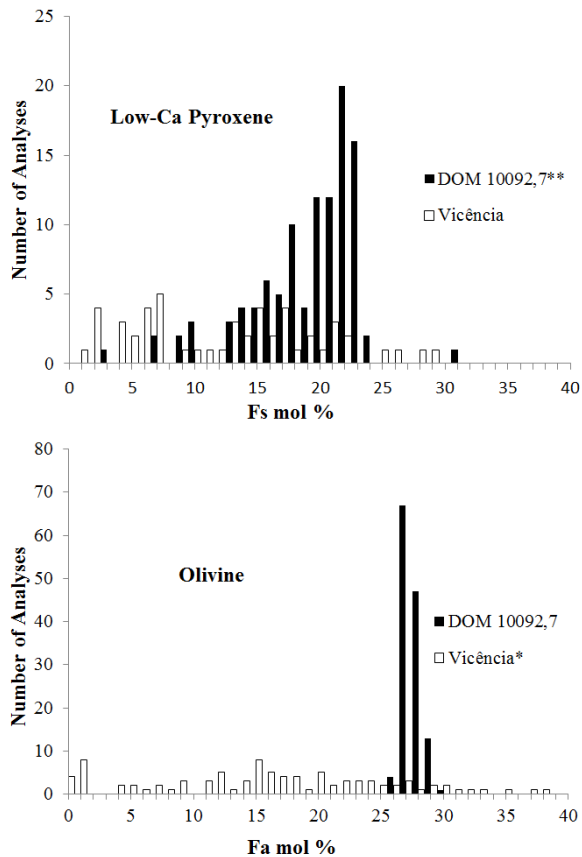


Figure 1: Compositional histograms of low-Ca pyroxene and olivine of DOM10092,7 compared to Vicência [3], a lightly shocked, LL3.2 ordinary chondrite. This shows the typical spread of a thermally unmetamorphosed LL chondrite compared to the data collected on this sample. Notice how the pyroxene data covers a wide range while the olivine data does not. **Data points above 40% Fs are excluded. *Matrix olivine data, which occurs above 40% Fs, is excluded.

kamacite. Taenite compositions range from 37-54 wt% Ni, with the rest of the mineral being made up of mostly Fe and small amount of Co and Cu (about 0.2 wt% and 0.3 wt%, respectively). The majority of compositions fall between 48-54 wt%, which is high for taenite found in most LL chondrites [4, 5]. The kamacite has an Fe content of 94-97 wt%, a Ni content of 2-5 wt%, and an average Co content of 1.6 wt%. The Co composition in the kamacite along with the mol% Fo in olivine is indicative of an LL chondrite [5]. There is <0.01 wt% P within the metals, which indicates P undersaturation.

This domain is made up of a fine grained matrix of sorts that surrounds many relic clasts of olivine and pyroxene (over 30%). At first glance, it appears to be a melt matrix that has begun to crystallize. However, at

higher magnification, especially in BSE images, one can see that the individual grains are anhedral and seem to be fragmented. They do not have a characteristic igneous texture of grains that have crystallized out of a melt. Also, there does not appear to be any glass or melt in between the grains, only empty space. Of those relics, there are 4 fragmental relics of barred olivine chondrules and 2 relics of radial pyroxene chondrules. The relics range in size from 10 μm to over 1 mm, the majority being a few hundred microns. The matrix-like grains are typically <1-10 μm . Typically, in impact melts, metals and sulfides form in blebs with metal globules surrounded by sulfide. This sample does not have this texture. Instead, the metal, when present, adjoins the sulfide edge and has more of a lithic or ingrown texture. Also, the metal in the sample does not have the zoned Ni abundances typical of metal entrained in impact melt. In contrast, the kamacite in DOM 10092 is randomly distributed and somewhat intergrown with taenite (Figure 3).

Metamorphic Conditions: *Thermal metamorphism.* We used the metamorphic classification scheme of Van Schmus & Wood [8] to classify this meteorite. The thermal metamorphism of the sample is difficult to narrow down. It has a narrow range of olivine compositions compared to a broad distribution of

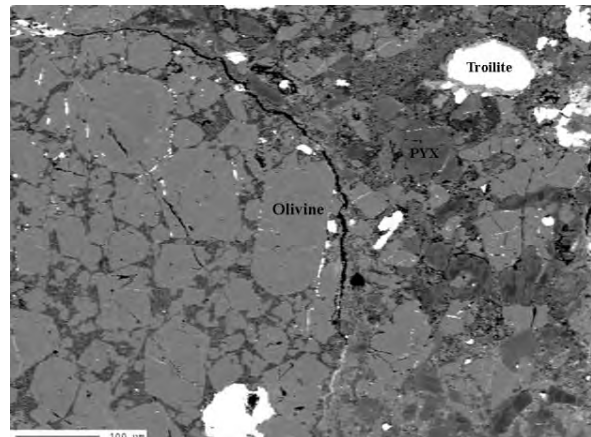


Figure 2: A good representative image of the clast fraction. Notice the large chondrule with euhedral olivine enclosed within. Notice how the spaces between olivine grains seem to be devitrifying. Also, notice the compositional zoning in the pyroxene. They contain areas of lighter grey (more Fe-rich) and darker grey (more Fe-poor) within the same grain. There is some troilite present. The small white veins are mostly alteration.

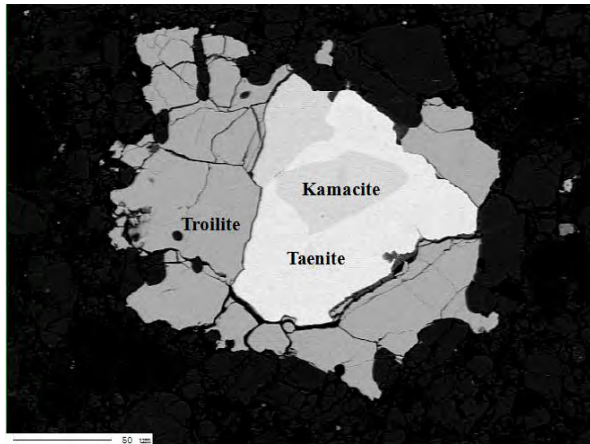


Figure 3: An example of one of the metal/sulfide grains labeled with their respective minerals. Notice the lack of a spherule shape and how kamacite seems to be at the core instead of taenite.

pyroxene compositions. The olivine compositions indicate at least type 4 metamorphism, whereas the pyroxene compositions indicate type 3. Also, when looking at the displacements of the composition peaks (Figure 1), one sees that the olivine is about 5% more Fe-rich than pyroxene. This is normal for LL chondrites, even well equilibrated ones [9]. The structural state of the pyroxene crystals also indicates a higher metamorphic state (type 5). At this time, we do not understand why the olivine and pyroxene compositions show different degrees of equilibration. The properties of the chondrule glass and the chondrule matrix glass indicate a type 3 or 4. This is not very reliable, though, since the glass can be very difficult to locate and much alteration has occurred. The overall chondrule sharpness indicates a type 4. Lastly, since the secondary feldspars are mainly microcrystalline aggregates seen with BSE images, this indicates a type 4 or 5.

Shock characteristics. Although the meteorite was originally classified as an impact melt breccia, it is clear that the shock state needed to be revisited. Using the criteria of Stöffler et al. [7], 20 olivine grains were analyzed for undulatory extinction (present), parallel planar fractures (present), mosaicism (not present), and melt areas (present). Based on those measurements, the sample has a shock state of S3 (weakly shocked). After looking at all of these criteria, we recommend classifying DOM 10092 as a type LL4 S3 ordinary chondrite.

Analysis of Results: The texture of the metals and sulfides is difficult to explain. The lack of spherules not only prevents a cooling rate from being determined, but it also is not typical in chondrites.

Also, this texture is not that of a plessite, which has wormy ingrowths of kamacite mixed with taenite. This texture has distinct taenite and kamacite zones (see Figure 3 again). For kamacite to exsolve out of taenite, the meteorite had to have cooled relatively slowly. The S3 shock state causes a post shock temperature increase of 100-150°C and a shock pressure of 15-20 GPa [7]. Depending on the temperature of the meteorite before impact, this may have been enough of an increase to reset the metal assemblages or possibly allow them to cool close to the temperature at which kamacite and taenite differentiate.

Conclusions: DOM10092 is an LL4 S3 ordinary chondrite. It has an interesting pyroxene composition distribution when compared to its olivine composition. Its metal and sulfide assemblages are also of interest. They do not contain the typical metal spherules but rather intergrown taenite and kamacite. This indicates slow cooling occurred at a lower temperature.

References. [1] Welzenbach L. et al. (2014) Antarctic Meteorite Newsletter, 37/1, 19. [2] Rubin, A. E. (2000) Earth-Sci. Rev. 50, 13. [3] Keil, K. et al. (2015) Meteoritics and Planetary Sci. 50, 6, 1089-111. [4] Taylor, G. J. & Heymann, D. (1971) Geochim. Cosmochim. Acta 35, 175-188. [5] Kring, D. A. et al. (1996) J. Geophys. Res., 101, 29, 253-29. [6] Clark, R. S. & Scott, E. R. D. (1980) Amer. Mineral. 65, 624-630. [7] Stöffler D., et al. (1991) Geochim. Cosmochim. Acta 55, 3845-3867. [8] Van Schmus, W. R. & Wood, J. A. (1967) Geochim. Cosmochim. Acta 31, 747-765. [9] Fodor, R.V. & Keil K. (1978) Spec. Publ. Univ. New Mex. Inst. Meteor., 19, 1-38.

GEOLOGY OF THE DEPOSITS OF THE LUNAR CRISIUM BASIN. M. U. Sliz^{1,2}, and P. D. Spudis²,
¹School of Earth, Atmospheric and Environmental Sciences, the University of Manchester, Oxford Road, Manchester, United Kingdom, M13 9PL; malgorzata.sliz@student.manchester.ac.uk, ²Lunar and Planetary Institute, 3600 Bay Area Boulevard, Houston, TX 77058.

Introduction: Crisium is a multi-ring impact basin of Nectarian-age, located in the north-eastern portion of the lunar near side [1]. The basin is morphologically complex, with some features suggesting that it was subjected to post-formation modification. Moreover, the size of Crisium basin has been subject to dispute; current best estimates conclude that the basin is about 1000 km in diameter. The geology of Crisium has been studied previously [2, 3] with aims to characterize the basin's composition and formation process. The high-resolution images from the Lunar Reconnaissance Orbiter and the Clementine mission allowed a more detailed study of this region of the lunar surface.

The aim of this project was to map the highland areas associated with the Crisium basin and other units present, with a focus on creating a basin-

centered geological map of the basin deposits. The remote sensing data used in completing the project included Lunar Reconnaissance Orbiter (LRO) images, Clementine maps of chemical composition and LOLA topographic maps. The new geological map of Crisium (Fig. 1) was used to study the composition and origin of the basin deposits which both can help to make inferences about the composition of the basin's crustal target. Moreover, the study of the Crisium basin's origin can contribute to the understanding of the processes behind formation of multi-ring impact basins on the Moon.

Method: LRO Wide Angle Camera (WAC) mosaic with resolution of 100 m/pixel has been used as a base map for the geological map of Crisium. The image mosaic was first converted to a basin-centered (18°N, 59°E) orthographic projection and geological

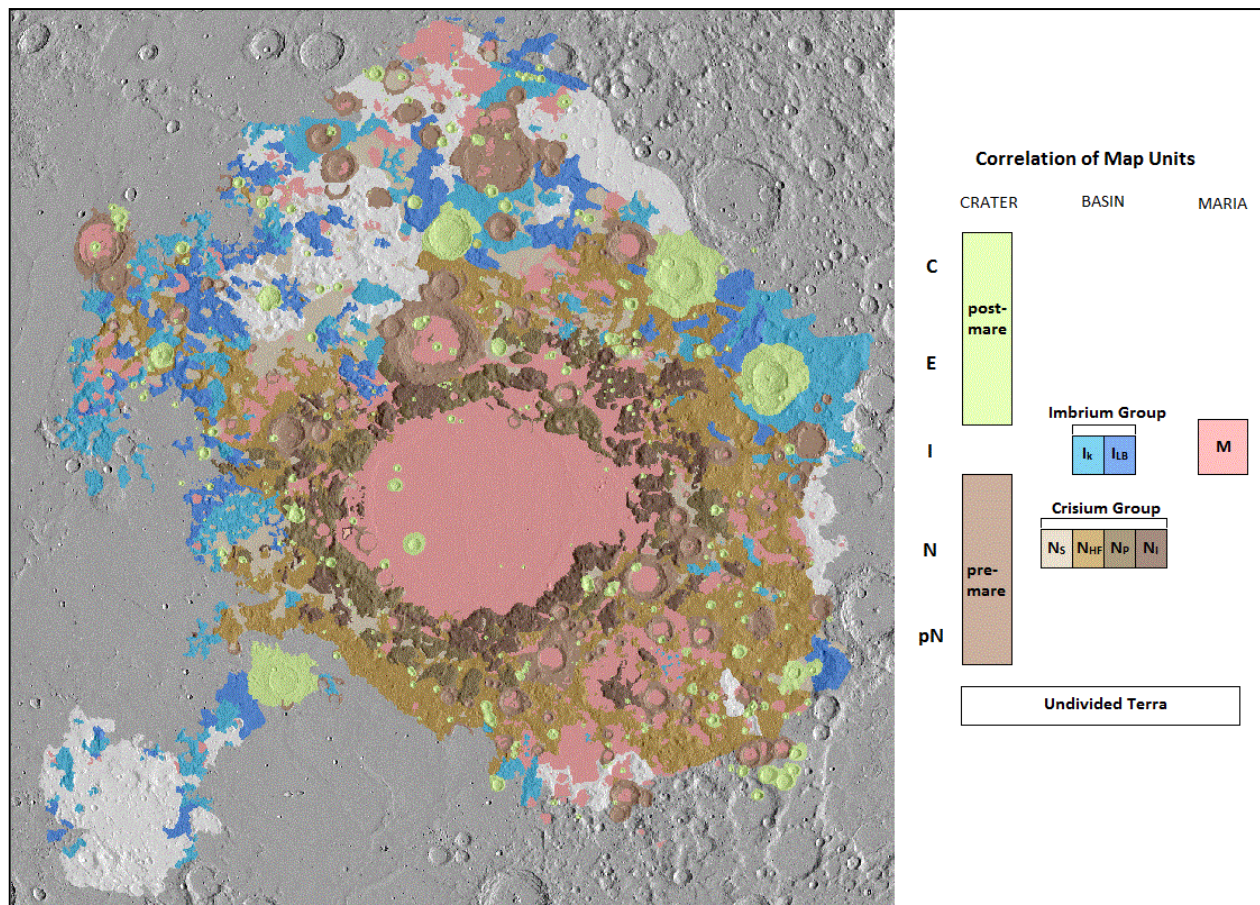


Figure 1. The new geological map of the Crisium impact basin. The approximate image dimensions are 1700 km in width by 1750 km in height.

units were added on top of the map in a series of layers using the ArcGIS ArcMap 10.1. Clementine FeO and TiO₂ and Lunar Prospector Th concentration maps, Clementine RGB false color map, as well as LOLA shaded relief and topography maps were co-registered with the base and used to characterize the Crisium basin units. The shaded relief and topography maps were especially useful in cases of units where unit boundaries were not clearly visible on the base map and to distinguish between units with similar characteristics, e.g. platform and irregular massifs. Ten separate basin units were defined on the basis of their surface texture, morphology, chemical composition, stratigraphic position, and location within the basin.

The geological map was subsequently employed in geochemical analysis to obtain statistics for each unit for elemental concentrations using Spatial Analyst tool in ArcGIS. The analysis provided mean elemental concentrations for each unit and for separate segments of each unit (Figs. 2, 3).

Results: Ten units were distinguished on the new geological map of the Crisium basin. In stratigraphic order from oldest to youngest, the units are: Undivided Terra, Pre-mare Crater Material, Irregular Massifs, Platform Massifs, Smooth Plains, Hilly and Furrowed Terrain, Mare Basalts, Lineated Basin Material, Knobby Material, and Post-mare Crater Material (Figs. 1, 2).

The Crisium Group comprises of the highland units associated with that impact basin. Its four members are: Irregular Massifs, Platform Massifs, Smooth Plains, and Hilly and Furrowed Terrain; all are Nectarian-age. The Irregular Massifs occur concentrically around the central mare within an approx. 460 km radius from the basin's center. The unit appears blocky with irregular peaks and is topographically higher than the majority of the

surrounding terrain. The Platform Massifs are similar to the Irregular Massifs in their blocky structure; however, these massifs show no sharp peaks but rather, appear to have flat tops, analogous to terrestrial mesas. Hilly and Furrowed Terrain extends up to 750 km radially from the center of the Crisium basin, and stands as a transition unit between the low-lying, flat mare basalts and the massif units.

The Imbrium Group consists of two members: Knobby Material and Lineated Basin Material. These lie beyond the second ring of Crisium at an approx. 385 km radius, and occupy predominantly the north-western portion of the basin. The Knobby Material has hummocky structure and comprises of irregularly shaped blocks. The Lineated Basin Material contains linear striae oriented in a direction radial to the center of the Imbrium basin. The majority of the unit is NW of the Crisium ring. Only one segment in the south-eastern portion of the Crisium basin shows an emplacement direction of NE-SW.

The craters in the Crisium basin region are divided into two categories: Pre- and Post-mare Crater Material. Pre-mare craters were classified as pre-Nectarian to early Imbrian and are heavily modified, with the majority possessing smooth, mare-filled floors. Post-mare craters are of late Imbrian to Copernican age. These craters have well-developed rims; some young ones still possess rays (e.g. Proclus crater).

The Mare Basalt unit comprises of all mare segments present within the Crisium basin and in its proximity. The most distant mare deposits were mapped at an approx. 940 km radius from the basin's center. The mare deposits are characterized by high FeO content and appear smooth, flat and dark.

Analysis: The Imbrium Group members were interpreted as material ejected during the formation of Imbrium basin and superimposed onto the older,

Unit	FeO (wt% ± 1σ)	TiO ₂ (wt% ± 1σ)	Th (ppm ± 1σ)
Hilly and Furrowed Terrain	9.1 ± 4.0	0.9 ± 0.7	1.4 ± 0.5
Irregular Massif	7.6 ± 2.8	0.6 ± 0.5	1.2 ± 0.3
Knobby Material	10.2 ± 4.5	1.2 ± 1.0	1.7 ± 0.5
Lineated Basin Material	7.6 ± 2.6	0.7 ± 0.8	1.7 ± 0.5
Mare Basalt	9.6 ± 3.9	1.3 ± 0.8	1.4 ± 0.5
Platform Massif	7.1 ± 2.0	0.5 ± 0.3	1.2 ± 0.3
Post-mare Craters	8.3 ± 3.6	0.6 ± 0.6	1.4 ± 0.5
Pre-mare Craters	8.9 ± 3.7	1.2 ± 0.5	1.3 ± 0.4
Smooth Craters	7.4 ± 3.0	0.4 ± 0.4	1.6 ± 0.5
Undivided Terra	9.2 ± 3.5	0.9 ± 0.8	1.4 ± 0.4
Whole Basin Average	8.5 ± 1.0	0.8 ± 0.3	1.4 ± 0.2

Figure 2. A table of average elemental concentrations of different units of the Crisium basin. The information was extracted from the Clementine FeO and TiO₂ maps and the Lunar Prospector Th map.

Crisium basin deposits. The Knobby Material (Fig. 3a) displays a compositional dichotomy between its northern and southern parts, with the former being mafic and the latter more feldspathic. East and South-East regions of Crisium are not largely populated by Knobby Material or the Lineated Basin Material, confirming the source of these materials to be the Imbrium basin.

Crisium's highland material (Fig. 3b) presents a feldspathic composition, with no clinopyroxene observed in the RGB Clementine map, as expected. South-eastern portion of the Hilly and Furrowed Terrain displays a wide range of FeO concentrations (4.29-16.82 wt%) which likely results from partial 'contamination' of the deposit by mare basalts of Mare Undarum and Mare Spumans.

On the western edge of Mare Crisium (NW of Yerkes) lies a system of fractures (Fig. 4). The deposit is easily distinguishable on the element maps, showing low FeO, Th, and TiO₂ concentrations – 8.51, 0.26, and 0.61 wt%, respectively. The feature's mineralogy shows no clinopyroxene (i.e. it is highlands material). Despite its location within the surrounding smooth mare lavas, this feature is an isolated, fractured deposit of compositionally distinct highland material. We believe this feature is a remnant of the Crisium basin melt sheet. As such, this deposit should be considered a high priority target for future lunar sample-return missions because it would enable accurate dating of the Crisium impact event, as well as determining the composition of the basin's crustal target. Similar features are also found near Lick crater in the south-western part of Mare Crisium. These features are analogous to the fractures present in the Orientale Basin's Maunder Formation, interpreted as the impact melt sheet of the Orientale basin [4].

Conclusion: An updated geological map of the Crisium Basin co-registered with element concentration maps allowed compositional studies of the mapped units. Two groups of units were distinguished – the Crisium Group and the Imbrium Group. The Imbrium Group was interpreted as ejecta from the Imbrium Basin formation. Using the Clementine compositional maps and the RGB false color map, a possible melt sheet remnant was recognized within Mare Crisium and is a candidate for future sampling missions.

References: [1] Spudis P. D. (1993) *Geology of Multi-Ring Impact Basins* Cambridge Univ. [2] Wilhelms D.E. (1987) USGS PP 1347 [3] Wilhelms and McCauley (1971) USGS Map I-703. [4] Spudis P. D. et al. (2014) *JGR* **119**, E004521.

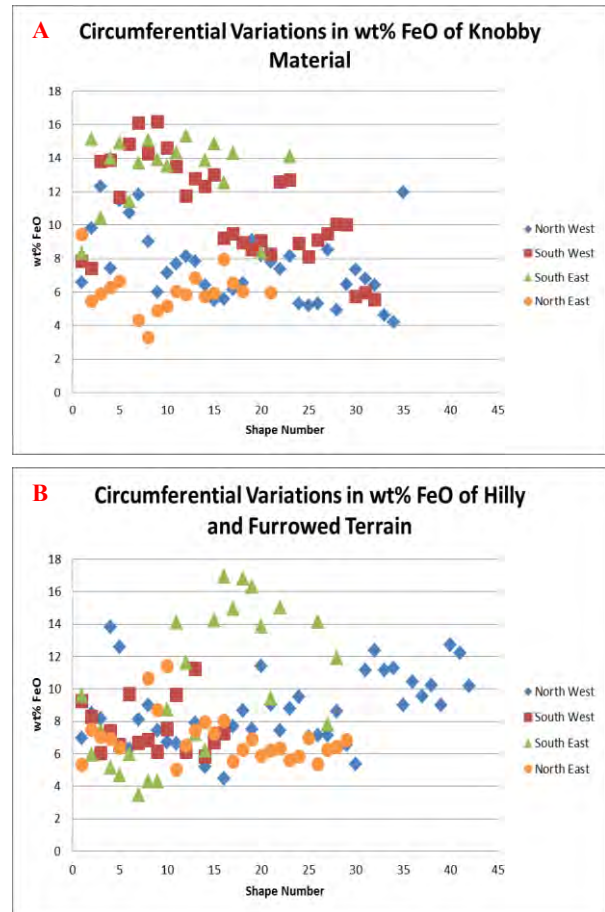


Figure 3. Plot of circumferential variations in FeO wt% of different Crisium deposits: (A) Knobby Material displays a clear division between the mafic portion in the South and feldspathic in the North; (B) Hilly and Furrowed Material displaying mostly a typical highland composition with a few mafic members in the South East and North West.

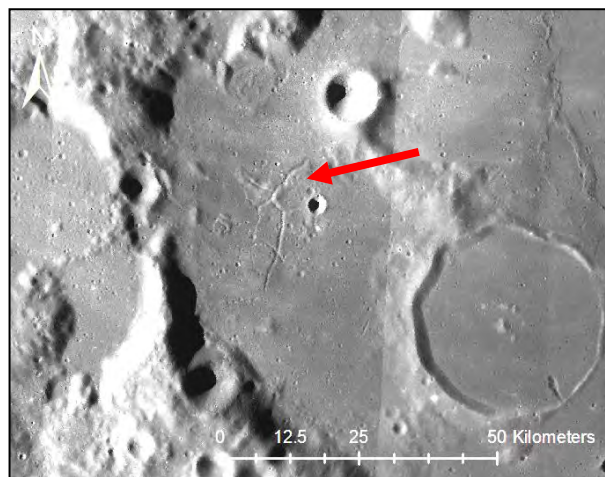


Figure 4. Location of the melt sheet in the Crisium basin (15°N, 50°E) indicated by the red arrow.

CHARACTERIZING RAYED CRATERS ON MERCURY AND GANYMEDE. J. Szczeszek¹, T. Hoogenboom², F. Scipioni², P. M. Schenk², K. Johnson³ and P. Byrne², ¹Adam Mickiewicz University in Poznan (Collegium Geologicum, ul. Maków Polnych 16, 61-606 Poznań); szczeszek@lpi.usra.edu ²Lunar and Planetary Institute, 3600 Bay Area Blvd., Houston TX 77058 ³Rice University, 6100 Main Street, Houston TX 77005.

Introduction: Crater rays are among the most conspicuous features on the Moon, Mercury and large icy satellites. These distinctive radial to sub-radial lineaments typically extend hundreds of kilometers from their source craters, and are readily identified by a contrast in albedo with respect to the overlain surface materials, especially when viewed at low phase angles (Fig. 1). Rayed craters constitute a group of craters that are least affected by other geological processes. Shoemaker and Hackman [1] first described the stratigraphic relation of the ray craters on the Moon and suggested that they are the youngest features because they superpose all other terrains. Recently, the surface of Mercury has been extensively observed by the MErcury Surface, Space ENvironment, GEochemistry, and Ranging (MESSENGER) spacecraft. Images taken from orbit show that Mercury is extensively cratered, with large-scale variations in crater density demarcating terrains by age. Yet the youngest population of impact craters, the so-called “rayed craters”, has been little studied so far. In this study we present the first comprehensive global catalog of rayed craters on Mercury and Ganymede. We compare these data to prior studies of rayed craters on the Moon, Mars, Iapetus, Mimas, Dione and Rhea [2-7], to better understand the formation of rayed craters in the inner and outer solar system. We analyzed spectral data to look for differences between the particular elements of rayed craters on Mercury.

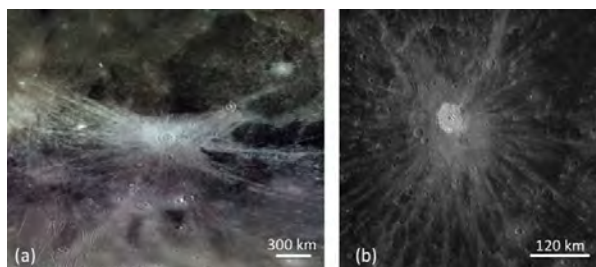


Figure 1: (a) Rayed crater on Ganymede (143 km in diameter) located at 39.19°S 85.51°W (b) Kuiper crater on Mercury (62 km in diameter) located at 11°S 31.5°W

Methods: We survey the total populations of rayed craters on Mercury and Ganymede using high-resolution global image and topographic data. For Mercury we examined the MESSENGER global monochrome mosaic map (250 m/pixel resolution) and the global mosaic 8-color map (665 m/pixel resolution).

In the case of Ganymede, we analyzed the global base map and color maps (1000 m/pixel resolution).

The image data were searched for craters which exhibited rayed ejecta extending multiple crater radii with higher albedo than the surroundings. The basic criterion for a “rayed” crater is one that has an ejecta deposit consisting of relatively bright (or dark) material or material of a distinctly different color radiating from its center and extending beyond the rim, like spokes on a wheel. Positively identified craters with diameter ≥ 2 km (data resolution limit) located between latitudes 60N to 60S were mapped by their crater rim using Arcmap. Beyond these limits, polar projections were utilized to improve diameter length measurements from distortion at the poles.

Our database includes rayed crater location (center latitude and longitude), distance from apex, diameter, crater morphology, bright-dark classification, and bright/dark ray lengths.

We investigated two spectral slopes - those between visible and infrared (VIS/IR) wavelengths (represented by ratio of the spectrum at 415nm versus the spectrum at 750 nm) and the slope UV/VIS (represented by the ratio 310nm/390nm). We used MASCA/VIRS (Visible and InfraRed Spectrograph) data in the visible range between 300 and 900 nm and 5 nm spectral resolution. For each rayed crater, we selected the available spectral data using the complete monochrome Mercury map with MASCS/VIRS Global color mosaic (QuickMap). We used averaged spectra for each element of each crater with available data.

Results: We mapped 160 rayed-craters on Mercury and 48 on Ganymede (Table 1). On Ganymede we find that 62.5% of rayed craters are located on the trailing side and the remaining 37.5% on the leading side. The limited rayed craters located on the poles (4 (~8%) on Ganymede and 5 (3.125%) on Mercury) may result from low illumination and sun angle issues making crater identification difficult.

Fig. 2 shows (i) cumulative crater frequency vs. diameter and (ii) R vs. diameter plots of our rayed crater catalog compared with rayed craters on Mimas, Rhea, Dione, Tethys, Mars and the Moon. On Mercury, we also mapped and cataloged 461 bright halo craters (which, like rayed craters are also thought to be relatively young). Mercury rayed craters and craters with bright halos fall into 2 different populations

(Fig. 2). We also found evidence of rays that kinked, but their origin remains enigmatic.

	count area (km ²)	# of rayed craters	Min. Diameter (km)	Max. Diameter (km)	Ave. Diameter (km)	Data
Mercury	74800000	160	1.81	111.63	19.72	Asia
Ganymede	87000000	48	10.75	142.59	52.08	Asia
Iapetus	17191.509	12	0.02	0.43	0.09	Schenk & Murphy 2011
Dione-reg	396909.4	88	0.18	2.49	1.01	Schenk & Murphy 2011
Dione-global	3997308.9	54	1.04	34.86	3.54	Schenk & Murphy 2011
Tethys	1191454.8	15	1.86	9.65	4.54	Schenk & Murphy 2011
Mimas	1324852.7	3	1.90	3.80	2.63	Schenk & Murphy 2011
Rhea-global	7334934.1	21	1.51	47.58	5.26	Schenk & Murphy 2011
rhea-mres-c	260433.07	7	0.42	4.25	1.45	Schenk & Murphy 2011
rhea-hres-e	84128.66	5	0.54	1.68	0.93	Schenk & Murphy 2011
rhea-hres-c	53403.41	21	0.16	1.04	0.37	Schenk & Murphy 2011
Moon	30980000	64	19.50	98.40	38.36	Grier et al. 2001
Mars	72399250	8	1.50	10.10	5.14	Tornabene et al 2006

Table 1: Rayed crater statistics comparison

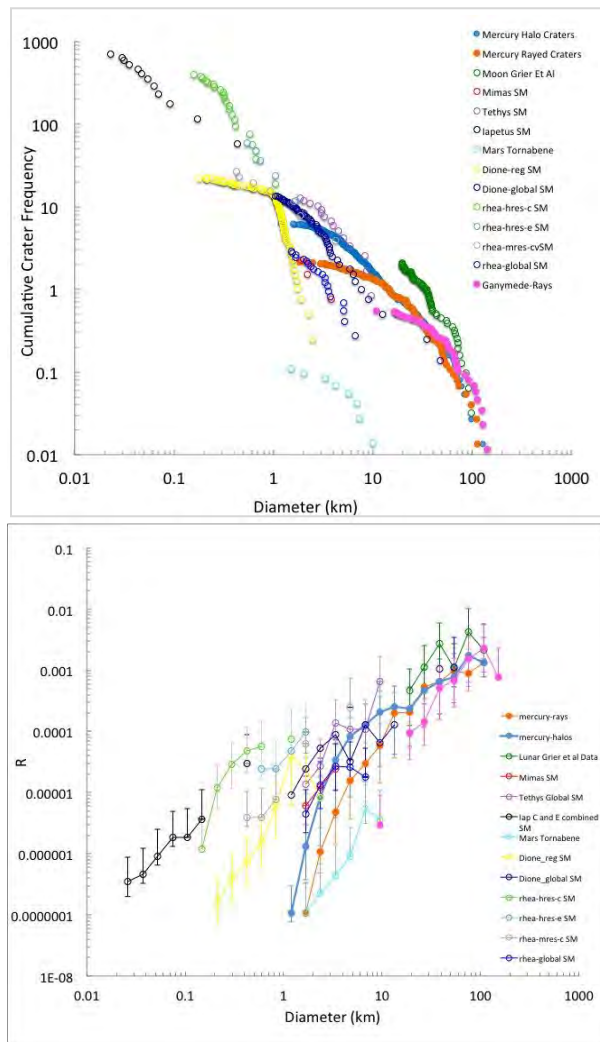


Figure 2 (i): Cumulative crater frequency vs diameter (ii): R vs. diameter comparative plot

Ray Lengths: On both Mercury and Ganymede, we found no clear dependence of maximum or average rays' length compared to crater diameter (as shown on Fig. 3). On both bodies, rays have similar length distributions. The crater with the longest rays (~707 km) is located in Mercury's northern hemisphere. Nevertheless Ganymede has significantly more rayed craters with diameter larger than 60km. This may indicate that rays are erased differently on Ganymede or that the population of current impactors is different.

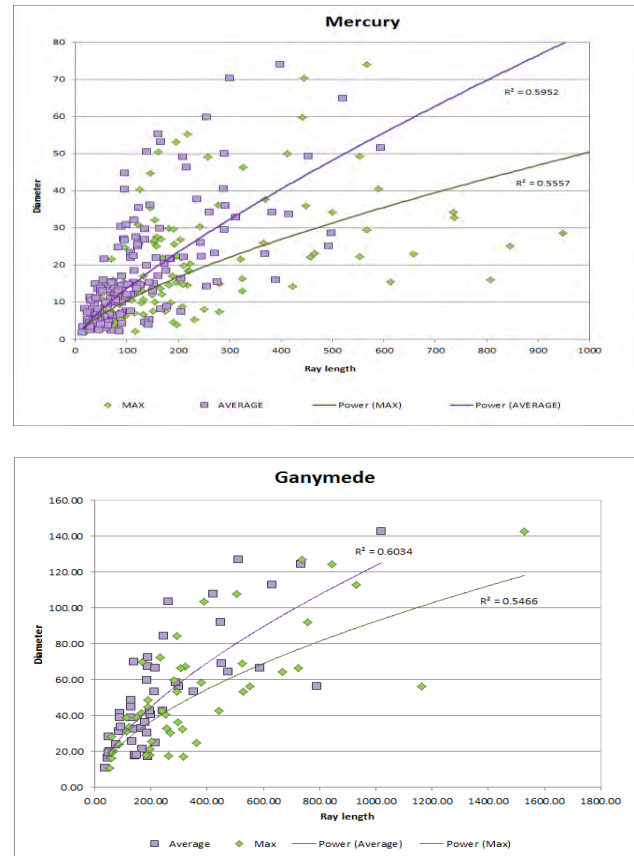


Figure 3: Diameter vs. length of rays measured on (a) Mercury and (b) Ganymede. Purple squares represent average ray lengths and green diamonds represent maximum ray lengths.

Mercury Spectra: We collected data for 69 rayed craters on Mercury (Fig. 4). As a general trend we observe a bigger spread in the UV/VIS plot. Mercury's spectrum is generally flat and shows a "red" spectral slope (Fig. 5) i.e. the reflectance increases with increasing wavelength [8].

We compared our results to Izenberg et al. [8]. Our data matches Mercury's average values that includes plains units that can be distinguished by morphology or visible-wavelength color. However, there is a sig-

nificant part that falls into red category, characterized by a higher reflectance and redder spectra than the planetary mean spectrum, while UVr (UltraViolet and Visible Spectrometer) and VISr (Visible and InfraRed Spectrograph) are lower. This part is represented mainly by pyroclastic deposits. There are also craters that fall into areas of high reflectance and morphologically fresh impact craters. Our results show a general trend of constant UV/VIS. Most of the crater components are clustered around the same values. Most of studied peaks' values overlap with their crater's centers, however not all of them follow this trend. Mercury's rayed craters spectrum is featureless. We confirm that spectra have a flat and red slope. In Fig. 5 we observe that even if the albedo level is different for the various components, all spectra are dominated by a steep red continuum. Further, we observe differences in the albedo levels between all crater components. The peak and rim overlap, meaning that they should have similar composition and/or grain size. The center has a steeper spectral slope, suggesting that its grain size may be bigger. We notice that different rays have different albedo levels. Variations in albedo level and the red trend are due to space weathering effects which darken the surface. Younger structures show higher albedo levels because space weathering effect acted for a shorter time.

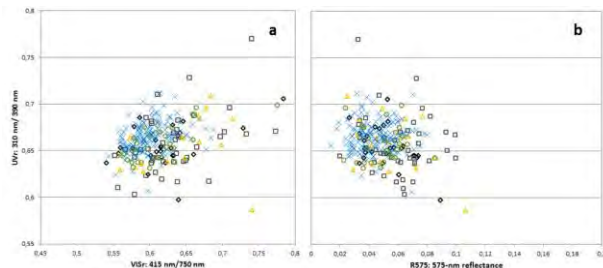


Figure 4: Mutual variation of spectral slopes for 69 rayed craters on Mercury's surface. (black = centers, gray = craters, yellow = peaks, green = rims, blue = rays)

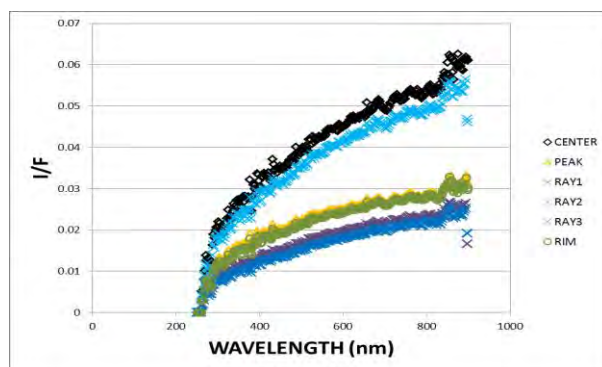


Figure 5: Spectra for Mercury's rayed crater (74km in diameter) located on Mercury at 32.37S, 170.38W.

Discussion: Great debate has arisen as to the source and flux of comets (and asteroids), the impact of which on these bodies is the sole means of estimating surface ages. Two main source populations have been proposed (we ignore asteroids as these are not dynamically important under current conditions). For a moon orbiting one of the outer planets, Zahnle et al. [9] confirmed that cratering rates by a heliocentric population should be much greater (by 10 to 40 times) on the leading hemisphere than the trailing. Conversely, a planetocentric population (dominated by secondary projectiles launched into Saturn orbit from these moons) will mostly return to the originating satellite [10]. Models show a weak 1:2 global cratering asymmetry for this “sesquinary” population favoring the hemisphere opposite the original source basin [10]. Such leading/trailing asymmetries in crater distribution have also been observed on Neptune's moon Triton (e.g. [9, 11, 12]. Schenk and Murphy [4] found that Dione and Tethys show significant enhancement in rayed crater density on the leading hemispheres by factors ~ 4 and a similar enhancement on Rhea (factor between 1 and 2). The factor of 1.67 higher rayed crater density on the leading side of Ganymede is less than predicted by [10] and less than that observed for craters generally, and much less than predicted for heliocentric projectiles [9]. This could be because the relative rates of surface alteration on the trailing and leading hemispheres, which are unknown, resulting in differential ray erasure. Further, small ray crater systems could fade away much faster than larger ones. Understanding this will require further work.

References: [1] Shoemaker, E.M., and Hackman, R.J., 1962, Academic Press, p.289–300. [2] Tornabene L. L. et al. (2006), J. Geophys. Res., 111, E10006, [3] Werner, S. et al (2014), Science: Vol. 343 no. 6177 pp. 1343-1346 [4] Schenk, P & S.W. Murphy, LPSC 2011, 2098. [5] Grier, J. et al. (2011), Journal of Geophysical Research, 106, E12 32847-32862. [6] Werner, S. & Medvedev, S. (2010) Earth and Planetary Science Letters 295(1-2), s 147- 158. [7] Herrick R. et al. (2011) Icarus, 215:452–454. [8] Izenberg, N. R. et al. (2014) Icarus 228, 364-374. [9] Zahnle, K. et al. (2001) Icarus 153, 111-129. [10] Alvarellos, J. et al 2005, Icarus 178, 104-123. [11] Shoemaker, E.M. et al (1982). in Satellites of Jupiter, ed.D. Morrison (Tucson: The University of Arizona Press), 435–520. [12] Schenk, P. & Sobieszczyk, S. (1999), Bull. Am. Astron. Soc., 31, 118. 136, 202–222.

LUNAR SWIRLS: INSIGHTS FROM PARTICLE TRACKING SIMULATIONS AT MARE MARGINIS AND NW OF APOLLO.

C. J. Tai Udovicic¹, G. Y. Kramer², E. M. Harnett³, ¹Department of Physics, University of Toronto, 60 St George St, Toronto, ON M5S 1A7, ²Lunar and Planetary Institute, 3600 Bay Area Blvd, Houston, TX 77058, ³Department of Earth and Space Sciences, University of Washington, 4000 15th Avenue NE, Seattle, WA 98195-1310.

Introduction and Background:

Lunar swirls are high albedo and optically immature surface features that appear at most of the Moon's magnetic anomalies (magnomalies) [1]. Although optical immaturity usually indicates younger lunar material, swirls do not appear to differ in age from adjacent optically mature soils [2]. Lunar swirls are best explained by the hypothesis presented by [3] that deflection of solar wind ions by magnomalies causes uneven space weathering of the swirl surface. We mapped the lunar swirls at Mare Marginis and NW of Apollo basin using multispectral data and analyzed them in the context of solar wind particle simulations. We compared these regions to previously analyzed swirls [2], and present the implications our work has for potentially undetected swirls.

Space Weathering and Nanophase Iron: "Space weathering" describes the active processes that affect an airless Solar System body as a result of continuous bombardment from solar wind and micrometeorites. These processes create nanophase iron (npFe⁰) through the reduction of ferrous iron in mafic minerals [2] [5]. Nanophase iron (npFe⁰) is responsible for darkening and reddening in visible to near infrared spectra [4] [5]. An optical maturity metric which takes advantage of these spectral effects is the OMAT parameter [6].

Lunar Magnomalies: All lunar swirls are found within lunar magnomalies, but not every anomaly contains swirls. The peak strengths of the magnomalies vary between 4 and 30 nT at the surface [7]. Swirls are not necessarily found at the strongest anomalies. The anomalies at Mare Marginis and Reiner Gamma have peak surface strengths of about 6 nT and 22 nT, respectively, and both show bright swirls. In contrast, Hartwig peaks at 12 nT and Crisium peaks at 23 nT, but neither contain recognizable swirls [7].

Coherence is a property of magnetic fields which can be used to assess how well a magnetic field keeps its shape over a vertical distance. Presently, the best magnetic field data has been recorded by orbiters at an altitude >15 km (e.g. Lunar Prospector) [8]. Incoherent magnomalies lose most of their complexity before reaching the orbiter's altitude, causing their fine morphologies to be lost.

Solar wind ion deflection/Magnetic shielding model: In the magnetic shielding model [1], incoming solar wind is deflected by the lunar magnomalies caus-

ing swirl surfaces to remain relatively optically immature over time. This model assumes that charged solar wind ions, mostly protons (H⁺), play a large role in space weathering. Many observations have supported this hypothesis including spectral observations from Clementine [2] and Moon Mineralogy Mapper (M³) [9]. These showed that deflection of the solar wind retards weathering on the swirl surfaces, while adjacent dark surfaces, dubbed "dark lanes", are weathered at an accelerated rate [2]. This can be attributed to a solar wind sorting effect taking place at the lunar magnomalies [9]. This model is supported by observations of deflected protons by mini-magnetospheres at lunar magnomalies, providing first-hand evidence of proton scattering at swirl locations [10] [11]. Furthermore, a suite of plasma particle simulations have provided supporting evidence, showing again that protons can be sorted by lunar magnomalies [12] [13].

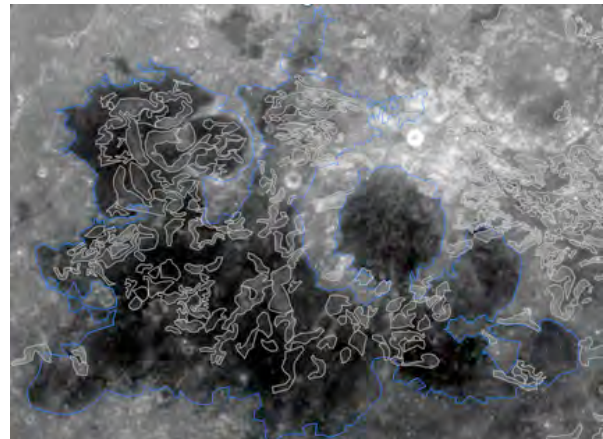


Fig 1: Marginis region. Swirls outlined in white, Mare marginis outlined in blue. LRO WAC 643 nm basemap. No swirls are found in Goddard basin (large centre) or Ibn Yunus (right of Goddard).

Method:

Lunar swirls are regions of anomalous albedo. Other lunar features such as fresh crater ejecta and sun-facing topography often have similar albedo anomalies and may appear in swirl-like sinuous patterns. We define swirls more practically as those high albedo features that are not otherwise explained by fresh impact craters, their ejecta, or lunar topography. We used a variety of datasets to distinguish the swirls in order to map Mare Marginis and NW of Apollo.

Mapping Marginis: The initial mapping of swirls at Marginis involved contrasting the Lunar Reconnaissance Orbiter Wide Angled Camera (LRO WAC) 643 nm normalized reflectance map [wms.lroc.asu.edu/lroc/view-rdr/WAC_EMP_NORMALIZED] with the LRO Global Lunar Digital terrain model 100 m (GLD100) [14] topographical map. These data were used in combination with LRO's Narrow Angle Camera (NAC) [15] to map the swirls at Marginis in detail. Although some swirls continue in the highlands east of this region, mapping was restricted to the mare and nearby highlands for the purpose of this study (Fig 1).

Mapping Apollo: Swirls NW of Apollo have been identified (e.g. [7]), but had not been mapped, likely because this heavily cratered highlands region has little contrast between swirl and background albedo, and the complicated topography causes albedo anomalies across the region. Mapping NW Apollo proved more difficult than Marginis so we incorporated other datasets including the Kaguya Multiband Imager (MI) [16], Clementine color-ratio [17], and a slope map derived from the WAC GLD100. The MI combined with the slope map provided improved contrast between high albedo swirls and high albedo slopes. Even so, only about half of the swirls located were found with this method. The rest were found using particle simulations as a guide.

Solar wind particle tracking: We modeled the interaction between the solar wind and the lunar magnomalies using the particle tracking simulations developed in [12]. These simulations have shown that magnomalies alone are sufficient to deflect incoming solar wind charged particles at Mare Ingenii, Reiner Gamma, and Gerasimovich [19]. The model uses surface field maps inverted from Lunar Prospector data [18]. The simulation launched 400,000 non-interacting test particles at both Mare Marginis (Fig 3) and NW of Apollo, and recorded the locations of those that impacted the surface. The generated maps of surface proton density and flux show areas of reduced proton flux coincided with regions of swirl formation. A major limitation of the particle tracking models is the magnetic field data. Currently, surface magnetic field models can predict a resolution of 0.1 degree per pixel [18], but swirls are often much smaller than these pixels and cannot be individually predicted by the models. Another limitation is the coherence of the magnomalies. Complicated and incoherent fields will have their fine structure essentially averaged out to the pixel resolution of the input fields. The particle simulations cannot resolve the vast majority of swirls which are smaller than the resolution of the magnetic field data, so they can only be used as a predictor for swirl-forming regions rather than individual swirls.

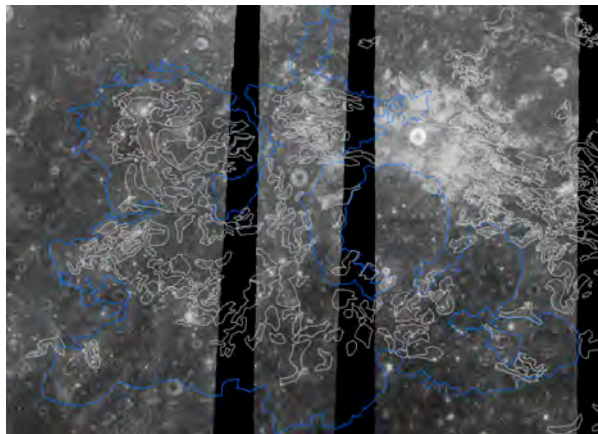


Fig 2: Marginis region. Swirls outlined in white, Mare marginis outlined in blue. Clementine UV/VIS OMAT basemap. Goddard appears darker (i.e. more optically mature) than nearby swirls outside the mare.

Discussion: Mare Marginis is a region of significant interest because of its prominent lunar swirls both on mare and highland soils. Marginis was chosen for this study to compare results of a similar region, Mare Ingenii, which was analyzed in [2]. Marginis is also interesting because of Goddard A, a fresh 11 km crater just north of Goddard, which ejected bright highlands material over the surrounding mare and highlands regions, both on swirl-rich and swirl-poor areas. Future work will include a full spectral analysis and comparison of fresh craters on- and off- swirl craters as well as soils for both the mare and highlands in the Marginis region.

The particle simulations for Marginis are shown in Figure 3 with the mare and swirl outlines overlaid. Swirls were found across the highlands and some of the mare regions, in locations where the particle simulations showed a decreased proton flux. Regions of increased proton flux tended to be lacking in swirls, while regions of decreased proton flux tended to be rich in swirls. The swirls were quite obvious in the regions of reduced proton flux in the low-FeO highlands. Locations of significant interest are the Goddard and Ibn Yunus basins in the center of the study region (see Fig 1). The model predicts a high proton flux across both mare-filled basins, and this is consistent with a lack of swirls within the basins (Fig 3). The target mare soils are rich in FeO with which to create $npFe^0$, causing the Goddard and Ibn Yunus basin floors to be weathered more efficiently than the nearby highlands. This effect is observable in the OMAT map where Goddard and Ibn Yunus appear dark (i.e. mature), while the surrounding highlands appear brighter (i.e. immature) and swirled. The presence of Goddard A makes this even more significant because its bright ejecta can be observed across the basin floors and in the surrounding highlands, but this clear OMAT difference still exists within the extent of its ejecta. This

is direct evidence that the ejecta which landed on mare soils are being weathered at an accelerated rate while those that landed on highland swirls are being preserved. This further supports the solar wind magnetic deflection model.

Applications to Apollo: We applied the same simulations to NW of Apollo and noticed that the previously mapped swirls appeared within areas of decreased proton flux as expected. We used the particle map to target other regions of decreased proton flux to search for swirls. This targeted search doubled our swirl count at NW of Apollo, pointing to several faint lunar swirls that had been overlooked by our previous mapping techniques.

Conclusion:

Preliminary analyses of the Marginis and NW of Apollo magnomalies show that swirl formation agrees with our particle tracking simulations. The clear inverse relationship between abundance of swirls and local proton flux functions as evidence for the magnetic shielding model and also as a predictor for swirl-forming regions. The mapping of NW of Apollo swirl region was enhanced by the particle simulations and we will seek to refine this method of predicting and locating swirls before examining mysterious magnomalies (e.g. Mare Crisium) which are devoid of swirls.

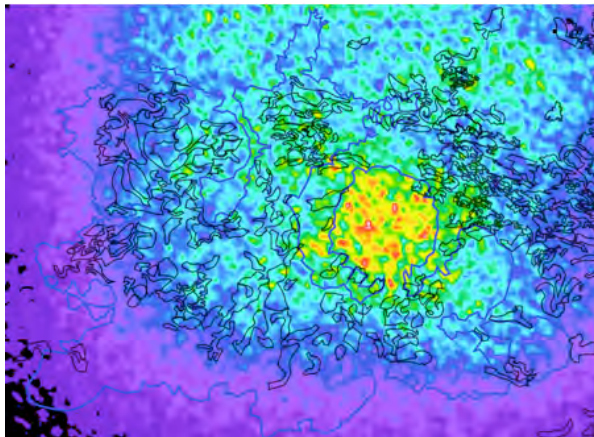


Fig 3: Marginis region. Swirls outlined in black, Mare marginis outlined in blue. Simulation proton flux results (particles $\text{cm}^{-2}\text{s}^{-1}$). Highest flux is centered over Goddard basin. Swirls are abundant in region of reduced flux NE of Goddard.

References: [1] L. L. Hood and C. R. Williams, "The lunar swirls: Distribution and possible origins," in Proc. LPSC, 1989, pp. 99–113. [2] G. Y. Kramer, "Characterization of lunar swirls at Mare Ingenii: A model for space weathering at magnetic anomalies," J. Geophys. Res., vol. 116, 2011. [3] L. L. Hood and G. Schubert, "Lunar magnetic anomalies and surface optical properties," Science, vol. 208, no. 4439, pp. 49–51,

Apr. 1980. [4] C. M. Pieters, et al. "Space weathering on airless bodies: Resolving a mystery with lunar samples," Meteorit. Planet. Sci., vol. 35, no. 5, pp. 1101–1107, 2000. [5] S. K. Noble, et al. "An experimental approach to understanding the optical effects of space weathering," Icarus, vol. 192, no. 2, pp. 629–642, 2007. [6] P. G. Lucey, et al. "Imaging of lunar surface maturity," J. Geophys. Res., vol. 105, no. E8, p. 20377, 2000. [7] D. T. Blewett, "Correction to 'Lunar swirls: Examining crustal magnetic anomalies and space weathering trends,'" J. Geophys. Res., vol. 116, no. E6, 2011. [8] L. L. Hood, et al. "Initial mapping and interpretation of lunar crustal magnetic anomalies using Lunar Prospector magnetometer data," J. Geophys. Res., vol. 106, no. E11, p. 27825, 2001. [9] G. Y. Kramer, et al. "M 3 spectral analysis of lunar swirls and the link between optical maturation and surface hydroxyl formation at magnetic anomalies," J. Geophys. Res., vol. 116, 2011. [10] M. Kurata, et al. "Mini-magnetosphere over the Reiner Gamma magnetic anomaly region on the Moon," Geophys. Res. Lett., vol. 32, no. 24, 2005. [11] R. A. Bamford, et al. "Minimagnetospheres above the lunar surface and the formation of lunar swirls," Phys. Rev. Lett., vol. 109, no. 8, p. 081101, Aug. 2012. [12] E. M. Harnett and W. Robert, "Two-dimensional MHD simulation of the solar wind interaction with magnetic field anomalies on the surface of the Moon," J. Geophys. Res., vol. 105, no. A11, p. 24997, 2000. [13] A. R. Poppe, et al. "Particle-in-cell simulations of the solar wind interaction with lunar crustal magnetic anomalies: Magnetic cusp regions," J. Geophys. Res., vol. 117, no. A9, 2012. [14] F. Scholten, J. Oberst, et al. "GLD100: The near-global lunar 100 m raster DTM from LROC WAC stereo image data," Journal of Geophysical Research: Planets, vol. 117, no. E12, 2012. [15] M. S. Robinson, et al. "Lunar Reconnaissance Orbiter Camera (LROC) Instrument Overview," Space Sci. Rev., vol. 150, no. 1–4, pp. 81–124, 2010. [16] M. Ohtake, et al. "Scientific objectives and specification of the SELENE Multiband Imager," Adv. Space Res., vol. 42, no. 2, pp. 301–304, 2008. [17] A. S. McEwen, et al. "Clementine observations of the aristarchus region of the moon," Science, vol. 266, no. 5192, pp. 1858–1862, Dec. 1994. [18] N. C. Richmond and L. L. Hood, "A preliminary global map of the vector lunar crustal magnetic field based on Lunar Prospector magnetometer data," J. Geophys. Res., vol. 113, no. E2, 2008. [19] E. M. Harnett and G. Y. Kramer, "Simulations of particle impact at lunar magnetic anomalies and comparison with spectral observations," in LPSC, 2014.

EVOLUTION OF SHOCK MELT COMPOSITIONS IN LUNAR REGOLITHS. A.M. Vance¹, R. Christoffersen², L.P. Keller², ¹Department of Geology, Beloit College, 700 College St, Beloit, WI 53511 (vancea@beloit.edu), ²NASA Johnson Space Center, 2101 NASA Parkway, Houston, TX 77058.

Introduction: Space weathering processes – driven primarily by solar wind ion and micrometeorite bombardment, are constantly changing the surface of airless bodies in our solar system [1]. The lack of atmosphere on the Moon means that the surface of the lunar regolith is being affected by these processes [2]. It is essential to study lunar soils in order to fully understand the processes of space weathering, and the skewing effects it has on optical reflectance spectral imaging of the lunar surface [1, 2].

Lunar *agglutinates* are aggregates of regolith grains fused together in a glassy matrix of shock melt produced during smaller-scale (mostly micrometeorite) impacts into the lunar regolith. They are a key product of lunar space weathering because the formation of their shock melt component involves reduction of FeO in the target material to generate nm-scale spherules of metallic Fe (nanophase Fe⁰) [3]. The ratio of elemental Fe, in the form of np-Fe⁰, to FeO in a given bulk soil indicates its maturity, and typically increases with decreasing grain size in a given soil [2,4].

The melting and mixing process in agglutinate formation remains poorly understood. The aim of this study is to further explore these processes by using sub-micron scale X-ray compositional mapping and image analysis to quantify the chemical homogeneity of agglutinitic glass, correlate its homogeneity to its parent soil maturity, and identify the principle chemical components contributing to the shock melt composition variations. An additional focus of the study was to see if agglutinates contain anomalously high Fe sub-micron scale compositional domains similar to those recently reported in glassy patina coatings on lunar rocks [5].

Samples and Method: The lunar soil samples were obtained from the curation facilities at Johnson Space Center. A polished grain mount of Apollo 11 soil, 10084 was used to develop and improve image analysis techniques. Data collection was done on pre-polished grain mounts of Apollo 17 mare soil samples 73241, 78501, 76281, and 78421, with approximately 16-21% Al₂O₃ and varying maturity (respective Is/FeO ratios: 18, 36, 45, 92) [6]. Back scatter electron images of agglutinitic glass were collected using the JEOL JSM-7600F field-emission scanning electron microscope. Quantitative element maps were collected by compositional spectrum imaging. The map pixels were quantified into values of wgt.% oxides, with pixel values in agglutinitic vesicles removed from the dataset. Numerical methods were devised to plot the oxide compositions of each onto ternary diagrams to create large, highly spatially resolved datasets showing mixing

trends and relationships of the glass.. Soil samples 73241 and 78501 were also characterized using the JSA-8530 field-emission electron probe microanalyzer in order to test the accuracy of the SEM data.

Results: Our image-based compositional analysis technique using the SEM yielded ternary variation diagrams similar to those obtained by microprobe, but with a factor of 10 to 100 higher density of points. Removal of data contained in pixels associated with holes was very effective, but it was generally not possible to remove the composition of entrained minerals from the dataset. The microprobe readings of both 73241 and 78501 showed plagioclase rich glass mixtures, with an Fe content above what was expected. These results are similar to those collected on the same areas using the SEM, which show that the SEM mapping technique can be used to accurately plot agglutinitic glass composition.

Under the SEM, it was possible to see that each agglutinate, regardless of maturity, contained agglutinitic glass that varied in homogeneity. There did not appear to be a higher proportion of homogeneous glass in the more mature agglutinates.

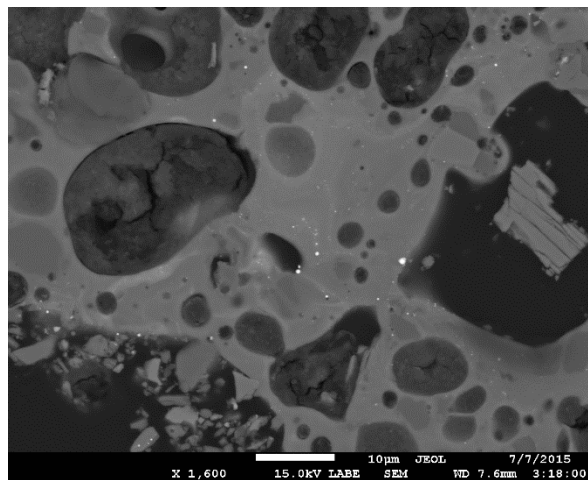


Figure 1. BSE image of agglutinitic glass in soil sample 73241_1,2 (Is/FeO: 18).

Agglutinates in the least mature soil, 73241 (Fig. 1, 3a-e), had dominantly Al₂O₃ rich glass, with a wide ranging TiO₂ component. The FeO content lies primarily on or above the mixing line of ilmenite and pyroxene (Fig 3c). The average glass composition of soil 78501 is Al₂O₃ rich, with a relatively low TiO₂ component (0-40%). The bulk of the FeO data lies well

above the ilmenite-pyroxene mixing line, with parts of the distribution extending to 100% FeO ranges. Soil 76281 has an Al_2O_3 rich average glass composition. The TiO_2 composition ranges from 10-80% from grain to grain. The FeO composition spans both below and above the mixing line of ilmenite and pyroxene.

The most mature soil, 78421 (Fig. 2, 3f-j), has a composition that fluctuates primarily between Al_2O_3 and MgO, with very little TiO_2 content (typically 0-30%). The FeO content plots on or above the ilmenite-pyroxene mixing line (Fig. 3h)

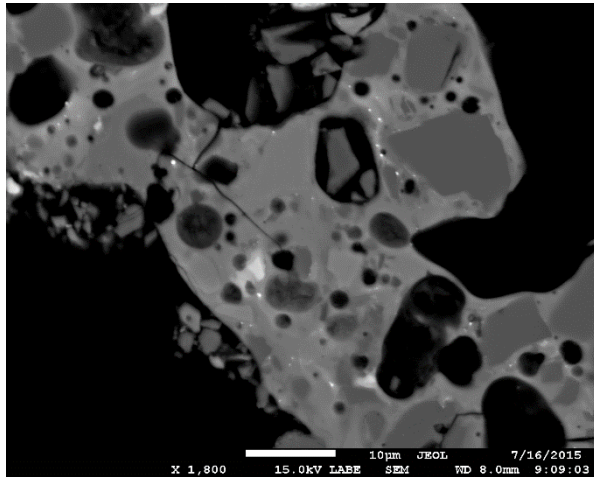
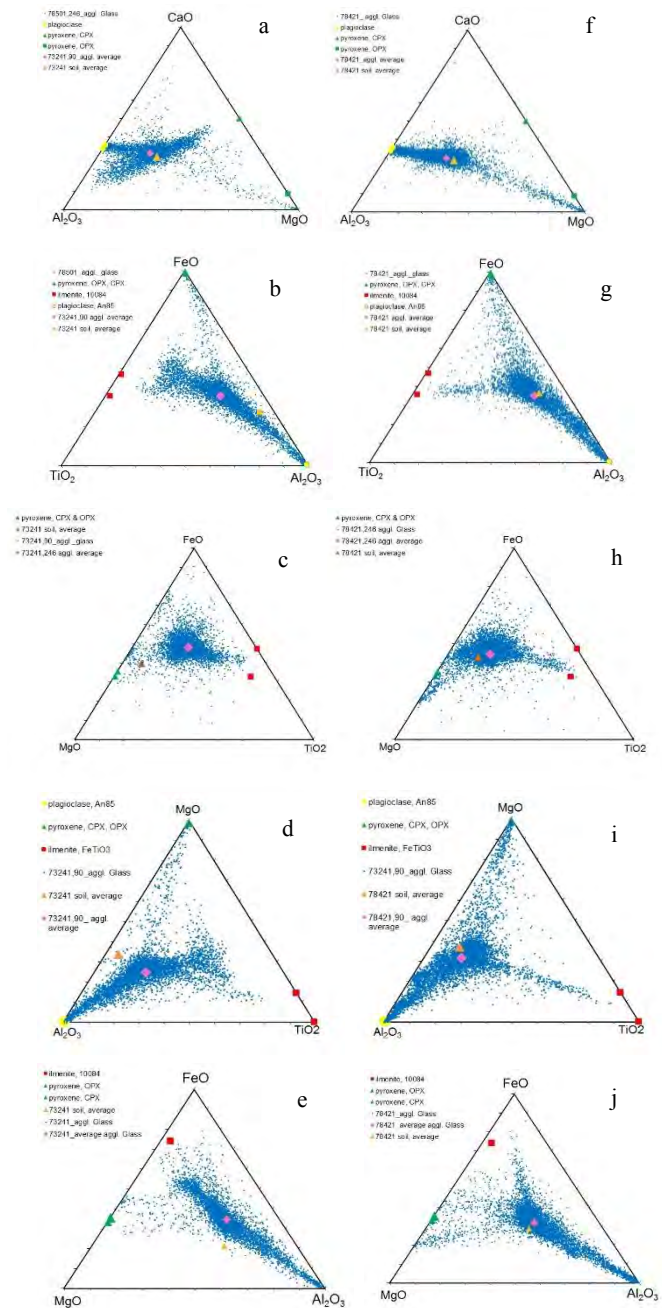


Figure 2. BSE image of agglutinitic glass in soil sample 78421_4,11 (Is/FeO: 92).

Discussion: The average melt composition across the samples is a plagioclase rich mixture with varying degrees of input from ilmenite and pyroxene. The plagioclase enrichment could reflect the greater susceptibility of this mineral to undergo shock melting, or modal variations in the regolith target [7].

Our results do not show a correlation between maturity and homogeneity. There was too much variation between individual grains in the same soil. However, this could be a result of the small number of glassy areas we looked at. The mapped regions were also chosen by visual inspection, and are not necessarily representative of the more intricate portions of agglutinitic glass in the grains.

The FeO content is consistently higher than the ilmenite-pyroxene mixing line in all samples (Fig. 3c,h) requiring another source of Fe contributing to the glass. By using standard normative subtractive measures, it is possible to calculate and plot the residual FeO, MgO and SiO_2 unassociated with either plagioclase or ilmenite, and contributed by pyroxene and olivine. These data (Fig. 4) show a unique compositional cluster which could be interpreted as having an olivine and pyroxene source, but overall has a much higher



Figures 3a-e. Compositional ternary diagrams of agglutinitic glass in least mature soil 73241. **Figures 3f-j.** Compositional ternary diagrams of agglutinitic glass in most mature soil 78421.

Fe/Mg ratio than typical lunar mare pyroxene and olivine compositions. There are several possibilities to explain this excess FeO over MgO. The first is that it is being derived from previously produced agglutinitic

glass, which is high in Fe. However, this does not explain where the high amounts of FeO in the original agglutinitic glass came from initially. Another option is that the FeO is coming from Fe deposits in the micrometeorite impactors. One final possibility is that these FeO anomalies are coming from Fe vapor rims, which are deposited around mineral grains during bombardment and loss of volatiles. These rims form primarily around grains in the finest fraction, which would support the fusion of the finest fraction theory [5,8,9]. The average Fe/Mg ratio of vapor rims found in patina is slightly higher than the residual values found in the agglutinitic glass. The low volume of Fe rich vapor rims indicates that there is most likely a combination of sources for the surprisingly large amounts of FeO.

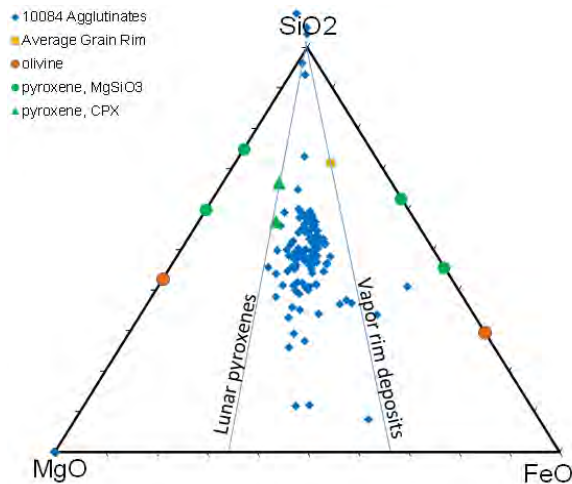


Figure 4. Plot of the residual FeO, MgO and SiO₂ in the agglutinitic glass of sample 10084

Conclusion: Agglutinate melting and mixing is a difficult process to model. Our results show that the chemical homogeneity of agglutinitic glass is not tied to maturity. The composition and homogeneity of the glass is determined by the target material, and individual mixing events are too stochastic to define parameters. It may be possible to better correlate homogeneity and maturity by sampling more soil samples.

The high FeO content of the glass indicates that ilmenite and pyroxene are not the only contributors to the composition. I believe that the residual FeO could be attributed to a mixture of melting high Fe pyroxene and olivine grains, and melting Fe vapor rim deposits around the finest fraction of soil grains. Further study of the vapor rim deposits would be necessary to confirm this hypothesis.

Acknowledgments: I would like to thank USRA and Lunar and Planetary Institute for this internship opportunity. I would also like to thank everyone at JSC who supported this research, especially Eve Berger and Kent Ross.

References: [1] Pieters, C. M. et al. (2000) *Meteoritics & Planet Sci.*, 35, 1101-1107. [2] Taylor, L. A. et al. (2001) *JGR*, 106, 27985-27999. [3] Shkuratov, Y. G. et al. (2007) *Solar System Research*, 41, 177-185. [4] Taylor, L. A. et al. (2000) *Meteoritics & Planet Sci.*, 36. [5] Christoffersen, R. et al. (2014) *LPS XXXV*, Abstract. [6] Morris, R. V. (1978) *Proc LPS Conf 9th*, Abstract, 2287-2297. [7] Schaal, R. B. and Hörz, F. (1980) *Proc LPS Conf 11th*, 1679-1695. [8] Papike, J. J. (1981) *LPS XII*, abstract, 805-807. [9] Walker, R. J., and Papike, J. J. (1981) *Proc LPS*, 12B, 421-432.



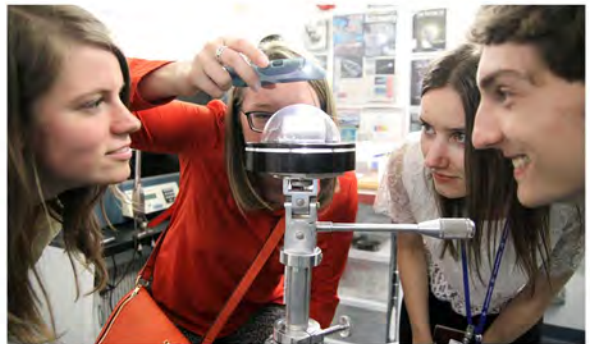
LPI Summer Intern Orientation June 1



JSC Stardust Lab and Lunar Curation Tour
Stardust, a NASA Discovery-class mission, was the first to return samples from a comet and from interstellar space.

Lunar Curation - The facility consists of storage vaults for the samples, laboratories for sample preparation and study, a vault for sample data and records, and machinery to supply nitrogen to the cabinets in which the samples are stored and processed.

June 1





Dr. Don Pettit is one of the most productive scientist-astronauts in the agency. He is the fourth most experienced American spacefarer of all time, with two long-duration stays aboard the International Space Station and a Space Shuttle mission. Don has also engaged in a six-week expedition to collect meteorites in Antarctica.

July 7



Meteorite Tour

The curation and collection of Antarctic meteorites is a U.S. funded, cooperative effort among NASA, the National Science Foundation (NSF) and the Smithsonian Institution. Meteorites of greater interest and undergoing detailed study are kept at JSC for distribution to the scientific community, but irons are sent directly to the Smithsonian Institution.

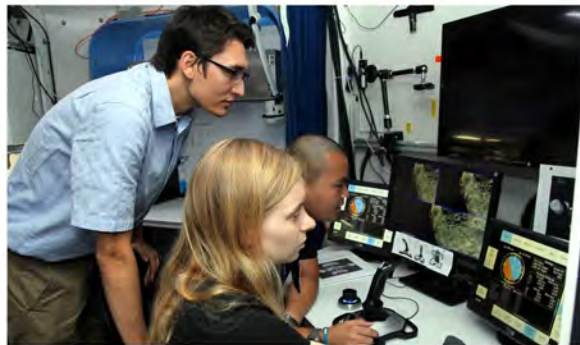
July 9



Human Exploration Research Analog (HERA) and Morpheus
 HERA, formerly known as the Deep Space Habitat, was transferred from the JSC Engineering Directorate to HRP in FY2013. The HERA will provide a high-fidelity research venue for scientists to use in addressing risks and gaps associated with human performance during spaceflight.

Morpheus is a NASA project to develop a vertical takeoff and vertical landing (VTVL) test vehicle called Morpheus Lander in order to demonstrate a new nontoxic spacecraft propellant system (methane and oxygen) and an autonomous landing and hazard detection technology.

July 16





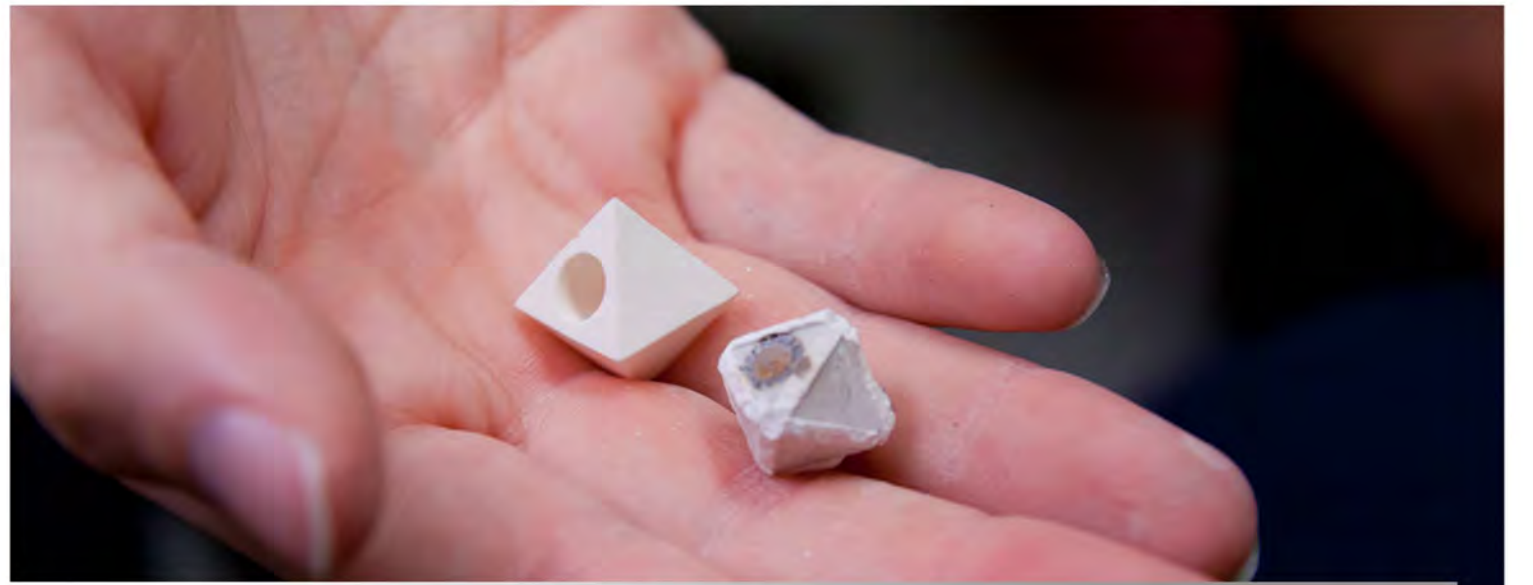
USRA BBQ July 11



Carrie McIntosh is extracting an experiment from the multi-anvil press. The experiment is part of a project investigating the partitioning of rare earth elements between lunar minerals and melts.



USRA BBQ July 11



A multi-anvil experimental assembly before (left) and after (right) an experiment carried out at 4 GPa. The assembly is compressed during the experiment and is smaller when extracted than the size it began.



Allison Vance was carbon coating her lunar soil sample, getting it ready to look at glass particles in the SEM.



Movie Night at USRA



Jessica Johnson is working on the JEOL JSM-7600F Electron Microscope, investigating an interesting foreign clast in an ordinary chondrite sample.



Chris Donaldson is investigating the cryogenic weathering of silicate minerals in regard to the formation of Mars' sulfate deposits.